Using quartz fabric intensity parameters to delineate strain patterns across the Himalayan Main Central thrust

Jesslyn K. Starnes [a],[*], Sean P. Long [a], Stacia M. Gordon [b], Jingyi Zhang [c], Emmanuel Soignard [d]

[a] School of the Environment, Washington State University, Pullman, WA, 99164, USA
[b] Department of Geological Sciences and Engineering, University of Nevada, Reno, NV, 89557, USA
[c] School of Mechanical and Materials Engineering, Washington State University, Pullman, WA, 99164, USA
[d] LeRoy Eyring Center for Solid State Science, Arizona State University, Tempe, AZ, 85287, USA

ARTICLE INFO

ABSTRACT

Disagreements over how to define shear zones within packages of pervasively recrystallized rock impede our ability to map and correlate these structures. Here, we explore a new approach for delineating the spatial extents of shear zones using quartz petrofabric, temperature, and kinematic data collected from two transects across the Main Central thrust (MCT) in western Bhutan. We calculated cylindricity, a fabric intensity parameter that has been previously interpreted as a proxy for finite strain magnitude, for each sample. Cylindricity values (measured on a scale from 0 to 1) increase upward from 0.11 to 0.47 between 2.3 and 1.3 km below the MCT, vary between 0.55 and 0.93 between 700 m below and 200 m above the MCT, and decrease upward from 0.68 to 0.37 between 2.4 and 11.7 km above the MCT. Fabric intensity increases with proximity to the MCT and defines a ~900 m-thick zone of elevated intensity that overlaps spatially with an interval of inverted metamorphism. Our results add to a growing number of recent studies that suggest that spatial patterns of fabric intensity, when integrated with temperature data and kinematic observations, can be used to delineate relative strain patterns across shear zones in the Himalaya and elsewhere.

1. Introduction

In contractional orogenic systems, motion on large-scale shear zones often accommodates a significant component of cumulative shortening. Understanding the deformation mechanisms, structural styles, and offset magnitudes of these major shear zones is fundamental for deciphering the tectonic evolution of an orogen. However, disagreements over how to best define shear zones within packages of rock that have been pervasively recrystallized, and in which gradients in finite strain (e.g., Simpson and De Paor, 1993) are not easily identifiable, impede our ability to accurately map and correlate these structures. For example, the Main Central thrust (MCT), a top-to-south shear zone mapped along the length of the Himalayan orogen, has been defined using several different criteria. These criteria include changes in lithology, isotopic signatures of footwall and hanging wall rocks, deformation temperature patterns, metamorphic mineral assemblages, and the conditions and timing of peak metamorphism (e.g., Gansser, 1983; Catlos et al., 2001; Robinson et al., 2001; Yin, 2006; Searle et al., 2008; Webb et al., 2013;

Long et al., 2016; Martin, 2016). Interpretations drawn from these different defining criteria have led to significant variation in the mapped position of the MCT (Martin, 2016).

A series of recent studies by Hunter et al. (2016a; 2016b; 2018; 2019) have demonstrated the potential for utilizing quartz petrofabric development (i.e., development of a crystallographic preferred orientation (CPO)) to identify zones of high strain in orogenic systems. The relationship between CPO development and strain magnitude has also been demonstrated in both modeling-based studies (e.g., Lister and Hobbs, 1980) and experimental studies (Barnhoorn et al., 2004; Heilbronner and Tullis, 2006; Muto et al., 2011; Wilson et al., 2019). Several field-based studies have also demonstrated that a correlation between CPO development and finite strain magnitude can occur in naturally-deformed rocks (e.g., Knipe and Law, 1987; Bhattacharya and Weber, 2004; Barth et al., 2010). In a recent study in Nepal, Larson et al. (2017) proposed that shear zone boundaries can be defined using statistical intensity parameters of quartz *c*-axis fabrics. This approach involves interpreting the intensity of fabric development as a proxy for

relative finite strain magnitude. Because finite strain magnitude is predicted to increase both in proximity to, and within, a shear zone (e.g., Ramsay and Graham, 1970; Simpson and De Paor, 1993), fabric intensities may be able to provide a quantifiable way to delineate the upper and lower boundaries of shear zones.

The goal of this study is to further test the applicability of this new approach, by collecting statistical indices of the intensity of quartz petrofabrics on two transects across the MCT in western Bhutan (Fig. 1). Importantly, previous interpretations of the location of the MCT in Bhutan, which are based on a variety of different defining criteria, have all resulted in general agreement on its location (Gansser, 1983; Bhargava, 1995; Grujic et al., 1996, 2002; Daniel et al., 2003; Long et al., 2011a, 2011b, 2016). This allows us to place our fabric intensity data within a rich context of lithologic, structural, kinematic, and temperature data, to compare how multiple datasets change with structural distance from the MCT. We present new mapping, petrofabric data, shear-sense observations, kinematic vorticity determinations, and deformation and peak temperature data from one transect, and combine new petrofabric intensity parameters with published kinematic and temperature data from the other transect (Long et al., 2016). We then explore the implications of this new approach for delineating strain patterns across the MCT, and shear zones in general, and discuss the benefits of using this method as part of a suite of quantitative datasets that provide a detailed structural context across shear zones.

2. Himalayan geologic background

The Himalayan-Tibetan orogenic system has formed from the Cenozoic collision and ongoing convergence of the Indian and Asian plates (e.g., Yin, 2006). Initial collision occurred at ~50–55 Ma (e.g., Rowley, 1996; Leech et al., 2005; Najman et al., 2012; Najman, 2006), and the Himalayan orogenic belt, which makes up the southern portion of the orogen (Fig. 1), began accommodating shortening at ~25 Ma (e. g., Gansser, 1964; LeFort, 1975; Mattauer, 1986; Yin and Harrison, 2000; Yin, 2006).

The Himalayan orogen has been divided into four tectonostratigraphic packages, which are separated by first-order structures that span the length of the orogen (Fig. 1) (e.g., Gansser, 1964; LeFort, 1975; Yin, 2006). To the south, unmetamorphosed, Neogene syn-orogenic sedimentary rocks of the Subhimalayan package overlie Quaternary foreland basin sediments across the Main Frontal thrust. Structurally above this, the Main Boundary thrust places greenschist-facies Precambrian to Paleozoic metasedimentary rocks of the Lesser Himalayan (LH) package over Subhimalayan rocks. LH rocks have been deformed into a south-vergent thrust belt that contains large duplex systems (e.g., Robinson et al., 2006; Long et al., 2011b; Webb et al., 2013). Moving northward, the Main Central thrust (MCT) places high-grade (typically upper amphibolite-facies) metasedimentary and meta-igneous rocks of the Greater Himalayan (GH) package over LH rocks. Finally, the Tethyan Himalayan package is a series of low-grade to unmetamorphosed Paleozoic-Mesozoic sedimentary rocks of the northern Indian margin on the northern edge of the Himalayan thrust belt. It overlies GH rocks across the top-down-to-north South Tibetan detachment system.

The MCT has long been considered to be one of the most important structures in the Himalaya (e.g., Gansser, 1964, 1983; LeFort, 1975; Grujic et al., 1996). The MCT was originally defined by the structurally-upward change in lithology from quartzite and schist of the LH package to gneisses of the GH package (e.g., Gansser, 1964). However, more recently, some researchers have defined the boundaries of the MCT on the basis of rheology and map the MCT at the transition from brittle-to-ductile deformation (e.g., Searle et al., 2008). The MCT has also been defined based on the age of shearing (e.g., Webb et al., 2013) or the age (e.g., Harrison et al., 1997) or conditions (e.g., Daniel et al., 2003; Long et al., 2016) of peak metamorphism above and below the fault. Not surprisingly, these different definitions have yielded differing interpretations for the location of the MCT across the Himalaya. For

example, in some transects in Nepal the structural position of the MCT varies by as much as ~5 km between different studies (Martin, 2016).
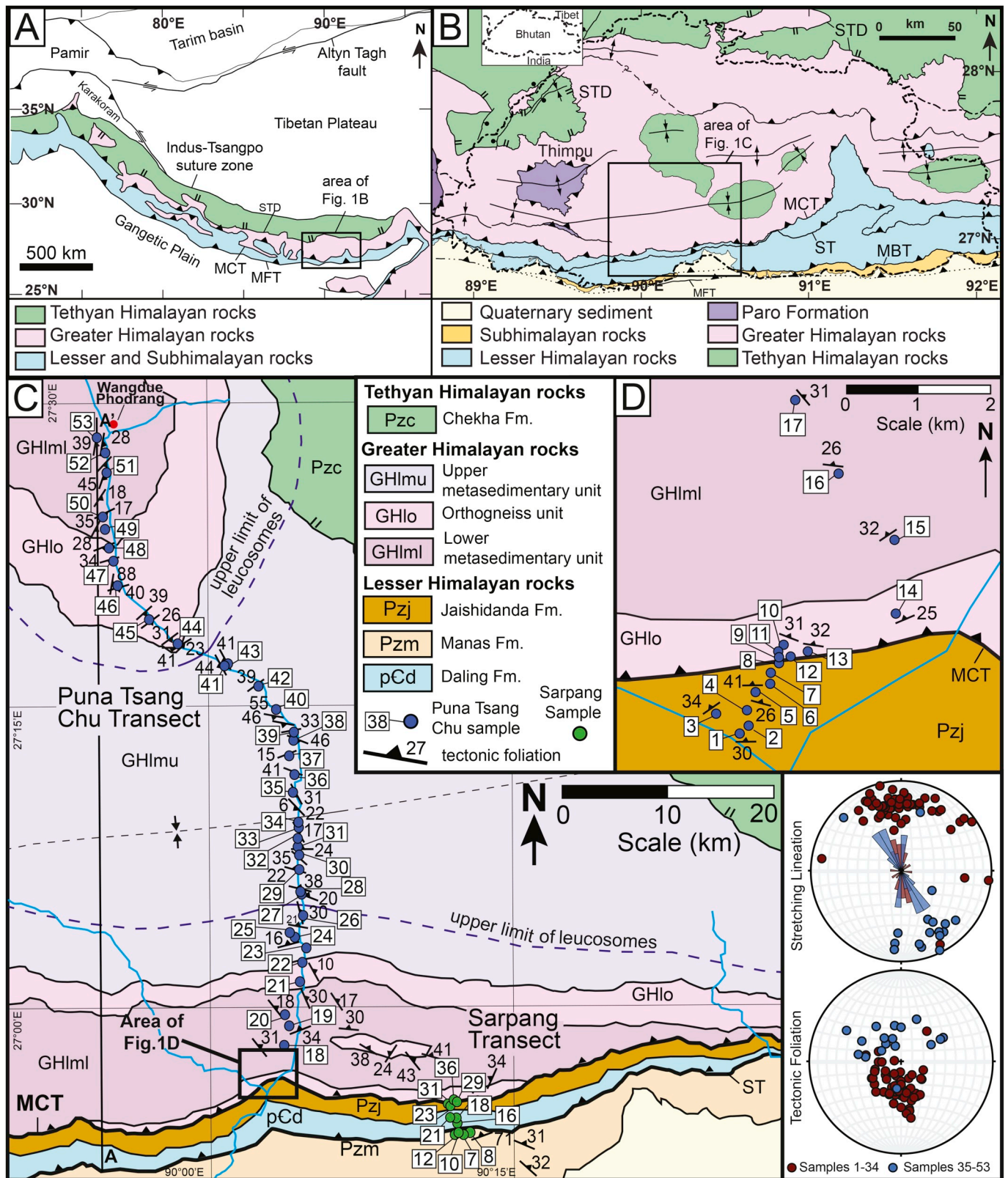
3. Tectonostratigraphy of Bhutan

Bhutan, which is located in the eastern portion of the Himalaya (Fig. 1), exhibits a similar first-order structural architecture to the rest of the orogen (e.g., Long et al., 2011b, 2011c). In western Bhutan, three LH units are mapped, the Manas Formation, Daling Formation, and Jaishidanda Formation. The Manas Formation is the structurally lowest LH unit and consists of coarse-grained, thick-bedded quartzite that is interlayered with dark-gray phyllite (Tangri, 1995; Long et al., 2011a, 2016). The Manas Formation has a minimum thickness of ~2100 m (Long et al., 2016) and is estimated to have a Neoproterozoic to Cambrian maximum depositional age range (Long et al., 2011b; McQuarrie et al., 2013).

The Daling Formation overlies the Manas Formation across the Shumar thrust (ST), a top-to-south thrust fault mapped along the length of Bhutan (Fig. 1B–C) (McQuarrie et al., 2008; Long et al., 2011b). The age of motion along the ST has been estimated between ~10 and 17 Ma in eastern Bhutan (Long et al., 2012) and ~9–15 Ma in western Bhutan (McQuarrie et al., 2014). The Daling Formation consists of thin-bedded, light gray to white quartzite, which is interlayered with dark green phyllite and schist (Dasgupta, 1995a; Long et al., 2011a). The Daling Formation is interpreted to have a Paleoproterozoic depositional age (Daniel et al., 2003; Richards et al., 2006; Long et al., 2011a). In our study area, the Daling Formation has a minimum structural thickness of ~1550 m (Long et al., 2016).

The Jaishidanda Formation lies above the Daling Formation across a contact that has been interpreted as originally depositional, but later deformed by pervasive shearing in the footwall of the MCT (e.g., Long et al., 2011a). The Jaishidanda Formation consists of interlayered gray, biotite-rich quartzite, and muscovite-biotite-garnet schist. In our study area, the Jaishidanda Formation exhibits a minimum structural thickness of ~800 m (Long et al., 2016). Detrital zircon from Jaishidanda quartzite samples collected along the length of Bhutan define a maximum depositional age range between Neoproterozoic and Ordovician (McQuarrie et al., 2008, 2013; Long et al., 2011a).

Above the MCT, the GH section has been divided into a lower metasedimentary unit (GHlml), an orthogneiss unit (GHlo), and an upper metasedimentary unit (GHlmu) (Long et al., 2011c). In our study area, GHlml exhibits a structural thickness of ~6500 m and consists primarily of interlayered garnet-bearing schist, paragneiss, quartzite, and orthogneiss, which contain granitic, layer-parallel leucosomes. On the basis of youngest detrital zircon populations and crystallization ages of orthogneiss bodies, the deposition of the sedimentary protoliths of unit GHlml is bracketed between Neoproterozoic and Ordovician (Long and McQuarrie, 2010; McQuarrie et al., 2013; Long et al., 2011b). Unit GHlo is an ~1000 m-thick section of granitic orthogneiss rich in feldspar augen, interpreted to represent Cambrian-Ordovician granite that intruded the sedimentary protoliths of GH rocks (Long and McQuarrie, 2010; Long et al., 2011b). Unit GHlmu is found at the structurally highest levels. It exhibits a minimum structural thickness of ~6000 m and is exposed within the hinge zone of a synform that can be mapped across much of western and central Bhutan (Fig. 1B) (Long et al., 2011b). Unit GHlmu is composed of interlayered garnet-bearing schist, paragneiss, and quartzite. The deposition of the sedimentary protoliths of unit GHlmu is bracketed between Neoproterozoic and Ordovician (Long and McQuarrie, 2010; Long et al., 2011b; McQuarrie et al., 2013).

The MCT, which places GH rocks over LH rocks, is estimated to have been active between ~23 and ~16 Ma in Bhutan (Long et al., 2012; Tobgay et al., 2012; McQuarrie et al., 2014). Previous studies in Bhutan have mapped the MCT at the top of the Jaishidanda Formation (e.g., Bhargava, 1995; Daniel et al., 2003; Long et al., 2011b, 2011c). This contact generally coincides with the structurally lowest appearance of aluminosilicate minerals, gneissic banding, and granitic-composition

Fig. 1. A) Simplified geologic map of the Himalayan-Tibetan orogen, showing tectonostratigraphic divisions of the Himalayan thrust belt (modified from Long et al., 2016). B) Geologic map of Bhutan showing first-order units and structures (modified from Long et al., 2012, 2016). MBT – Main Boundary thrust, MCT – Main Central thrust, MFT - Main Frontal thrust, ST – Shumar thrust, STD – South Tibetan Detachment. C) Geologic map of the Puna Tsang Chu and Sarpang transects, showing structural measurements and sample locations. Inset shows equal-area stereonets of all measurements of tectonic foliation (poles to planes plotted) and lineation (poles plotted) (generated using Stereonet 10; Allmendinger et al., 2011). D) Zoomed-in portion of the geologic map showing closely spaced samples and measurements collected in proximity to the MCT on the Puna Tsang Chu transect.
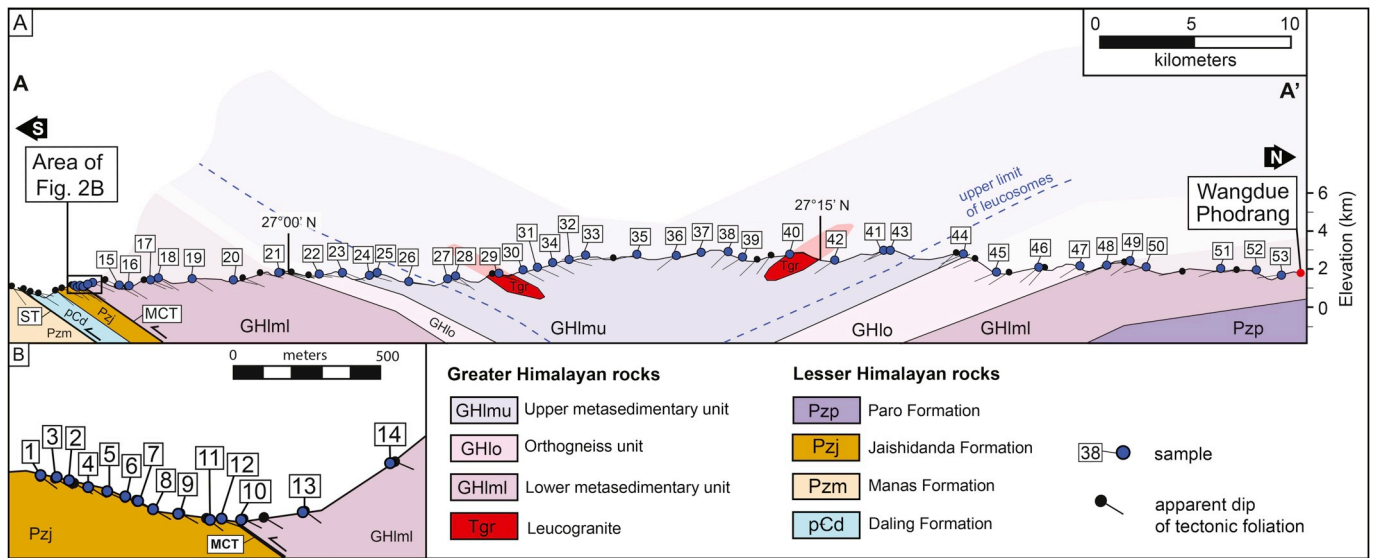
Fig. 2. A) Cross section of the Puna Tsang Chu transect showing sample locations and apparent dip of foliation measurements. B) Zoomed-in portion of the cross section showing closely spaced samples and measurements collected in proximity to the MCT.

leucosomes, which lie in close proximity to each other (often within the same outcrop, or within a few 10's of meters structural thickness) (e.g., Long et al., 2011b, 2011c). Most previous studies have mapped the position of the MCT at a similar location in Bhutan (e.g., Gansser, 1983; Bhargava, 1995; Grujic et al., 1996, 2002; Daniel et al., 2003; Long and McQuarrie, 2010; Long et al., 2011b, 2011c, 2016). However, the structural thickness of rocks involved in shearing during motion on the MCT remains enigmatic (Long et al., 2016). It is this aspect that we hope to address in this paper.

4. Transects across the MCT in western Bhutan

We collected data from two transects across the MCT in western Bhutan, the Puna Tsang Chu and Sarpang transects (Fig. 1C). We present new mapping, kinematic observations, quartz fabric data, and temperature data from the Puna Tsang Chu transect. Similar datasets were collected from the Sarpang transect by Long et al. (2016); here we present new fabric intensity parameters for Sarpang transect samples.

4.1. Puna Tsang Chu transect

The Puna Tsang Chu transect extends N–S for approximately 60 km (Fig. 1C), beginning just above the ST, crossing the MCT, and extending northward through a ~12 km-thick section of N-dipping GH rocks. The northern half of the transect crosses structurally downward through nearly the entire GH section within the S-dipping limb of a regional-scale synform (Long et al., 2011b). A total of 69 outcrops were examined, with samples collected at 55 localities (see Supplementary Material (SM) for a complete list of samples). The apparent dips of tectonic foliation were plotted on a cross section through the transect (Fig. 2), in order to calculate structural (i.e., foliation-normal) thicknesses. Most outcrops exhibit mineral stretching lineations, which have an overall average N-NNW or S-SSE trend (Fig. 1C inset). All map units, lithologies, and samples are projected onto a tectonostratigraphic column (Fig. 3), which are plotted according to structural height relative to the mapped reference position of the MCT (note that Fig. 3 plots samples projected from relative foreland and hinterland positions that span up to a ~60 km N–S distance). Rocks examined on the Puna Tsang Chu transect span a total structural height between −560 m and +12,300 m. In the text below, structural heights listed with negative numbers refer to structural distance below the MCT, and those with positive numbers refer to structural distance above the MCT.

All LH samples on the Puna Tsang Chu transect were collected from the uppermost ~525 m of the Jaishidanda Formation (Fig. 3), which consists of quartzite interlayered with biotite-garnet schist. The uppermost ~20 m of the Jaishidanda Formation (Fig. 4) exhibits several features that previous workers in Bhutan have interpreted as criteria defining the MCT, including the structurally lowest appearance of kyanite (sample 10D, −21 m), gneissic banding (sample 9C, −6 m), and leucosomes (sample 11A, 0 m). The contact between the Jaishidanda Formation and overlying GH rocks is mapped as the structural reference position of the MCT and is here delineated by the structurally lowest occurrence of granitic leucosomes.
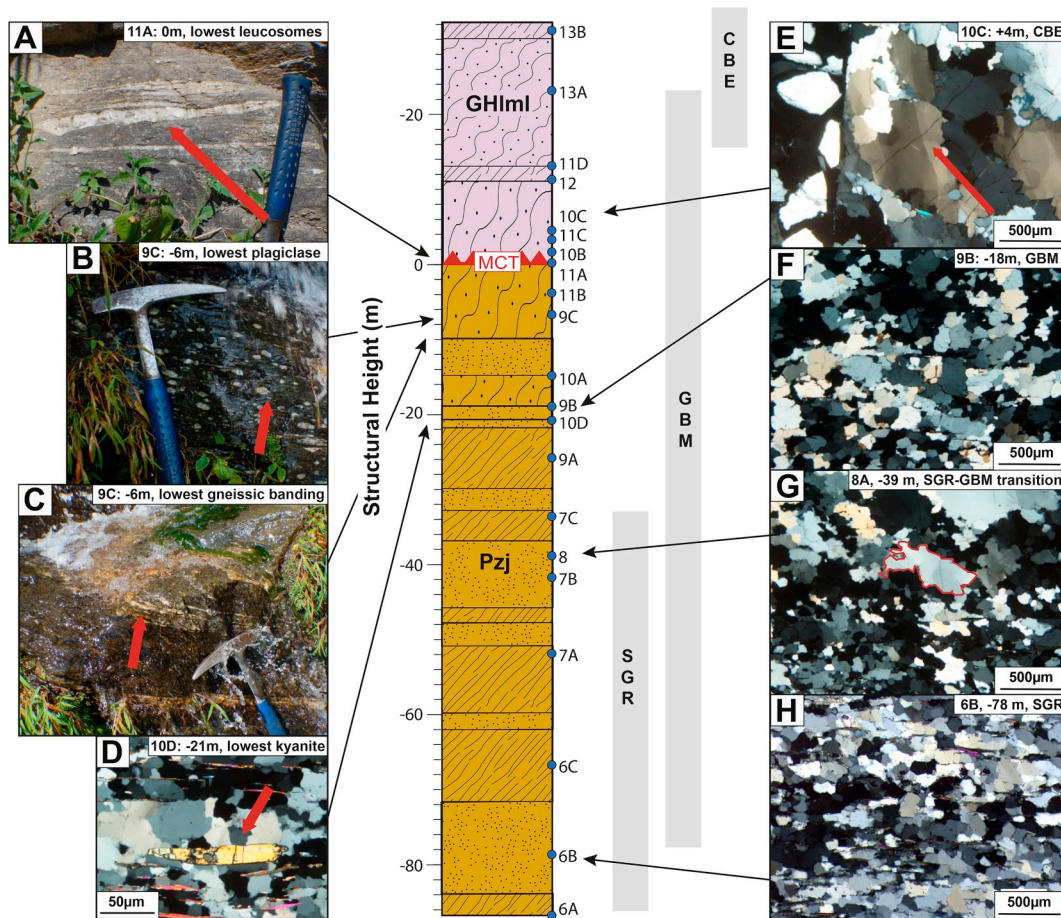
Above the MCT, the Puna Tsang Chu transect crosses through units GHlml, GHlo, and GHlmu. All three units are exposed in both limbs of a regional synform (Fig. 1C). GHlml is 6400 m-thick in the southern limb and has a minimum thickness of 3400 m in the northern limb. GHlml is dominated by biotite-, garnet-, and locally kyanite-bearing paragneiss that typically contains foliation-parallel, locally-deformed granitic leucosomes, and is interlayered with biotite-garnet schist and quartzite. GHlo is 800 m-thick in the southern limb of the synform and 3400 m-thick in the northern limb, and consists primarily of migmatitic, granitic orthogneiss. A minimum thickness of 6000 m of unit GHlmu is exposed and is dominated by biotite-garnet schist and biotite-rich quartzite. Within unit GHlmu, kyanite is absent above +8000 m, leucosomes are absent above +8800 m, and garnet is not observed above +9800 m, suggesting an overall upright metamorphic field gradient.

4.2. Sarpang transect

The Sarpang transect is located ~15 km to the east of the Puna Tsang Chu transect (Fig. 1C). Long et al. (2016) presented a detailed description of the Sarpang transect and collected peak temperature (RSCM and garnet-biotite thermometry), deformation temperature (quartz *c*-axis opening angle thermometry, quartz recrystallization temperature ranges), shear-sense, finite strain, and kinematic vorticity data. In this study, we calculate intensity parameters from the nine published petrofabric analyses of Long et al. (2016) and present fabric analyses from two new samples.

The portion of the Sarpang transect that extends from 2700 m below to 675 m above the MCT is shown on Fig. 5, and crosses two major shear zones, the MCT and the structurally-lower ST (Long et al., 2016). LH rock units include the Manas, Daling, and Jaishidanda Formations. The Manas Formation consists of light-gray quartzite and dark-gray phyllite.

Fig. 3. Tectonostratigraphic column of the Puna Tsang Chu transect, showing units, lithologies, samples, shear-sense observations, peak and deformation temperature data, cylindricity, m-index values, and c-axis pole plots. Mineral abbreviations after Whitney and Evans (2010). MCT – Main Central thrust.

Above this, the ST places a ~1500 m-thick section of tan to white quartzite and green phyllite of the Daling Formation over the Manas Formation. The ST corresponds with the lowest observed occurrence of biotite porphyroblasts. A structural thickness of 800 m of the Jaishidanda Formation overlies the Daling Formation and is dominated by biotite- and garnet-bearing schist and quartzite (Long et al., 2016). Garnet first appears at −675 m, and plagioclase porphyroblasts appear at −75 m. The contact between the LH and GH rocks is marked by the appearance of migmatitic, granitic orthogneiss; this contact is mapped as the structural reference position of the MCT. Above this contact, GH

Fig. 4. Tectonostratigraphic column of the Puna Tsang Chu zoomed into the mapped location of the MCT, showing field photographs of outcrop-scale observations and photomicrographs (cross-polarized light) of quartz recrystallization microstructures. A) Stop 11A (0 m), the site of the structurally lowest occurrence of granitic leucosomes. B) Stop 9c (−6 m), which exhibits the structurally lowest occurrence of plagioclase porphyroblasts. C) Stop 9c (−6 m), which contains the structurally lowest observed gneissic banding. D) Sample 10D (−21 m), which contains the structurally lowest kyanite observed on the transect. E) Sample 10C, showing multiple extinction domains within a large amoeboid quartz grain that intersect at right angles, which is characteristic of chessboard extinction (CBE). F) Sample 9b, showing large (≥0.5 mm) amoeboid quartz grains that are characteristic of grain boundary migration (GBM) recrystallization. G) Sample 8A, showing large amoeboid 'island grains' (one is highlighted in red) within a matrix of small (≤∼50 μm), polygonal quartz neoblasts characteristic of subgrain rotation (SGR) recrystallization. This is interpreted as a transitional texture between GBM and SGR recrystallization (e.g., Stipp et al., 2002). H) Sample 6B, showing an equigranular texture of small (≤∼50 μm) polygonal quartz neoblasts characteristic of SGR recrystallization.

rocks consist of migmatitic orthogneiss, paragneiss, schist, and quartzite.

5. Quartz petrofabrics

Quantitative analyses of quartz petrofabrics are frequently utilized to understand the deformation history of recrystallized, quartz-rich tectonites (e.g., Bouchez and Pecher, 1981; Carreras and Celma, 1982; Law et al., 1990, 2004; 2011, 2013; Pennacchioni et al., 2010; Hunter et al., 2016a, 2018; 2019; Larson et al., 2017). Data gleaned from quartz c-axis pole plots can be used to determine shear-sense, constrain the style of 3-D strain, estimate kinematic vorticity, and bracket deformation temperature (e.g., Kruhl, 1998; Wallis, 1992, 1995; Law et al., 2004; Morgan and Law, 2004; Passchier and Trouw, 2005; Faleiros et al., 2016). Here, we also explore the utility of using statistical intensity parameters calculated from quartz c-axis fabrics to provide insight into strain patterns across shear zones, by testing this method on a known location of the MCT.

We collected the orientations of quartz c- and a-axes using electron backscatter diffraction (EBSD) analysis of foliation-normal, lineation-parallel thin sections. MTEX, an open-source Matlab toolbox (Bachmann et al., 2010; https://mtex-toolbox.github.io/), was used to analyze and reduce the resulting data using a one-per-pixel analysis (i.e., one orientation data point per individual pixel), to produce c-axis pole plots (Fig. 6), grain orientation maps (see SM for supporting figures), and grain counts. MTEX was also used to quantify fabric intensity by calculating cylindricity (B) (Vollmer, 1990) and the M-index (M) (Skemer et al., 2005) (see SM for methodology). Cylindricity measures an orientation tensor that is calculated by matrix summation of three-unit column eigenvectors that represent the orientation of each crystal (Vollmer, 1990), while the M-index compares the distribution of misorientation angles between crystals in a sample with the expected distribution of misorientation angles in an ideally random fabric (Skemer et al., 2005). In addition to cylindricity and the M-index, several other parameters for measuring fabric intensity are available, including the J-index (Bunge, 1982). However, our chosen indices are ideal because they are not sensitive to the number of grains in each analysis (e.g., Bunge, 1982; Skemer et al., 2005; Mainprice et al., 2015). Both B and M are listed as unitless values between 0 and 1 (a random fabric and a perfectly non-random fabric, respectively). Recent work has demonstrated that the intensity of fabric development has been shown to spatially correlate with high strain zones (Hunter et al., 2016a, 2018; 2019; Larson et al., 2017, 2018). Therefore, M and B values may be interpreted as proxies for relative strain magnitude (Larson et al., 2017),
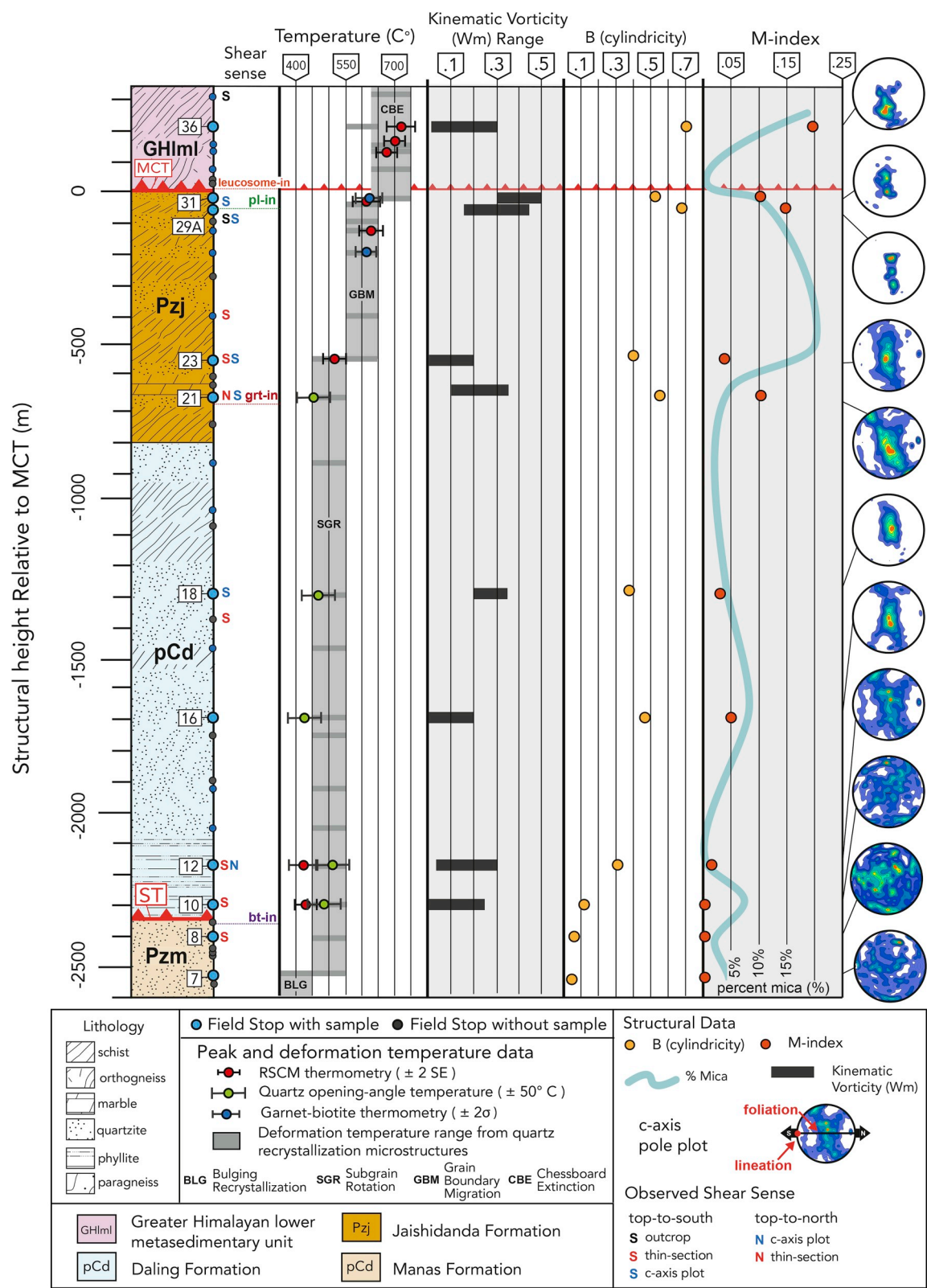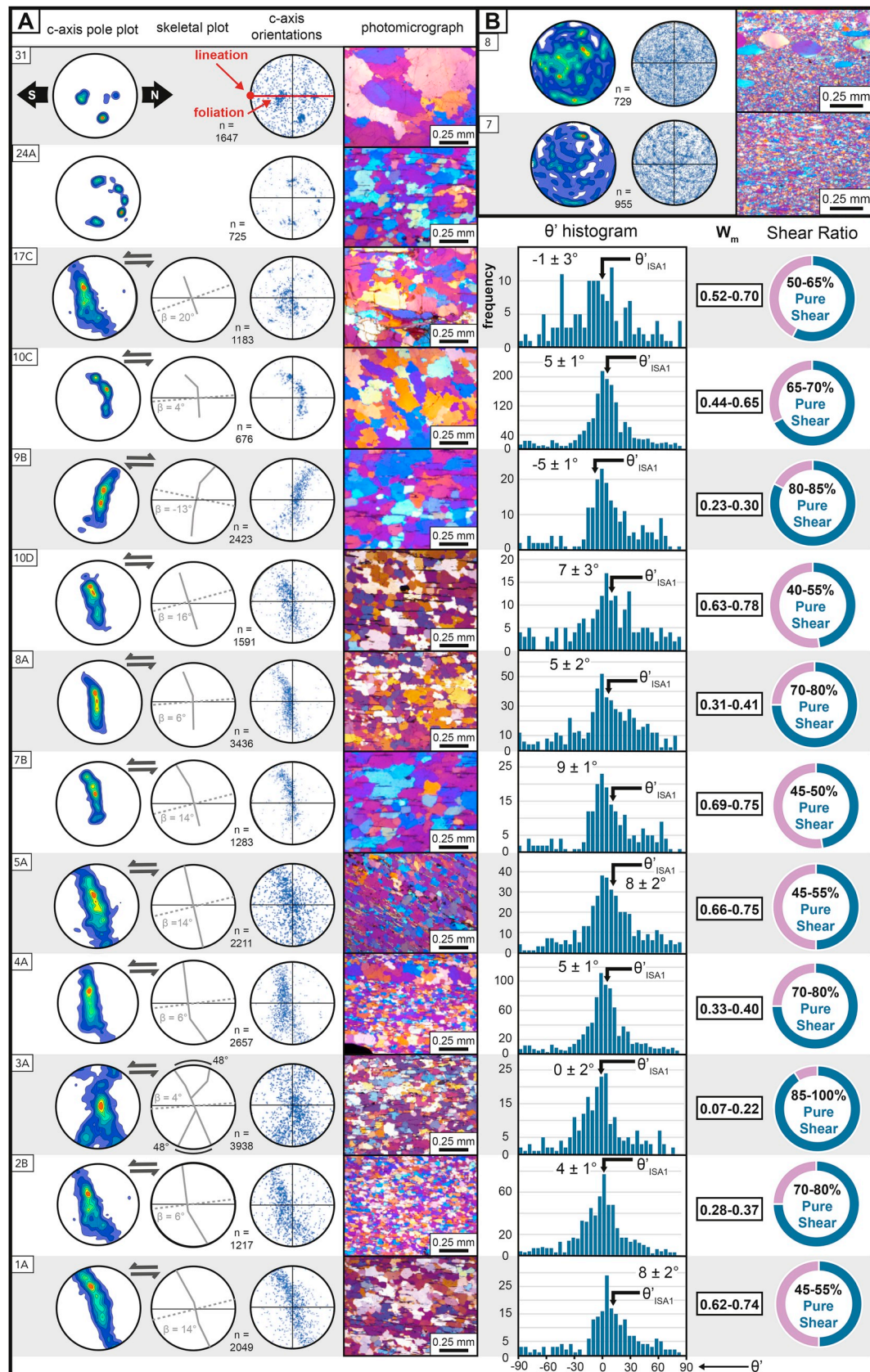
Fig. 5. Tectonostratigraphic column of the Sarpang transect (modified from Long et al., 2016), showing unit divisions, lithologies, samples, shear-sense observations, peak and deformation temperature data, cylindricity, m-index values, and c-axis pole plots. Mineral abbreviations after Whitney and Evans (2010). MCT – Main Central thrust, ST – Shumar thrust.

Fig. 6. Quartz petrofabric data from: A) the Puna Tsang Chu transect (n = 13) and B) the Sarpang transect (n = 2), including contoured *c*-axis pole plots, visually interpreted *c*-axis skeletal plots (which also list *β* angles), individually plotted *c*-axes, photomicrographs taken with a 540 nm *λ* plate inserted, histograms of θ frequency used to calculate θ′$_{ISA1}$, and the percentage of pure shear indicated by kinematic vorticity data.

with higher intensity fabrics indicative of greater relative finite strain.

On the Puna Tsang Chu transect, EBSD analyses were conducted on thirteen quartzite samples that ranged between −520 m and +11,500 m, with all but three of the samples clustered tightly between −520 m and +5 m (Fig. 3). All samples except for the structurally-highest two (samples 24A and 31A, at +7600 and + 11,700 m, respectively) exhibit *c*-axis pole plot patterns that define a strong CPO (Fig. 6). Ten of these samples exhibit single-girdle patterns, which are interpreted to form from a combination of prism <a>, rhomb <a> slip, and basal <a> slip (Bouchez, 1978; Bouchez et al., 1983; Lister, 1977; Lister and Hobbs, 1980).

B and M values from the Puna Tsang Chu transect define an overall pattern of higher-intensity (i.e., more ordered) fabrics with proximity to the reference position of the MCT (Fig. 3; Table 1). Samples between −520 m and −160 m (n = 5) yielded B values of 0.82, 0.70, 0.61, 0.85, and 0.59 (in order of ascending structural height), indicating relatively ordered fabrics. Samples between −45 m and +5 m (n = 5) yielded higher B values of 0.91, 0.90, 0.86, 0.91, and 0.93, indicating highly non-random fabrics. Samples collected at +2.4, +7.5, and +11.7 km yielded B values of 0.68, 0.52, and 0.37, respectively, indicating decreasing fabric intensity with increasing structural height above the MCT. M values are overall lower, with a cumulative range between 0.02 and 0.34, but demonstrate a nearly identical trend with structural height as the B values (Fig. 3; Table 1). Samples between −520 m and −160 m yielded M values between 0.08 and 0.20, samples between −45 m and +15 m yielded M values between 0.23 and 0.34, and samples at +2.4, +7.5 and + 11.7 km yielded M values of 0.27, 0.12, and 0.02.

On the Sarpang transect, eleven quartzite samples have been analyzed for quartz petrofabrics, and span structural heights between −2600 m and +200 m (Fig. 5; Table 1). Petrofabric data for the nine structurally-highest samples were originally presented in Long et al. (2016), and data from two additional samples (7 and 8), which lie below the Shumar thrust (ST), were collected in this study. These two new samples lack evidence for a clearly-defined CPO, exhibiting a nearly random distribution of *c*-axes (Fig. 6B). The five structurally-lowest samples of Long et al. (2016) (samples 10, 12, 16, 18, and 21), which are spread between −2300 m and −675 m, yielded crossed-girdle patterns. Moving structurally higher, samples 23 and 29A, collected at −550 m and −75 m, yielded single-girdle patterns, and samples 31 and 36, collected at −25 m and +200 m, yielded center point maxima.

We calculated B and M values for all 11 samples on the Sarpang transect. The two samples collected below the ST (7 and 8) yielded B values of 0.05 and 0.07 and M values of 0.01 and 0.00 (Fig. 5), respectively. This defines a lack of fabric development, which is corroborated by partial recrystallization observed in thin sections of Manas Formation quartzite (Long et al., 2016). Above the ST, six samples spread between −2200 m and −550 m exhibit a general increase in fabric strength with increasing structural height, with B values that increase gradually upward from 0.12 to 0.55, and M values that correspondingly increase from 0.0 to 0.11 (Fig. 5). Samples collected at −75 m, −50 m, and +200 m yielded higher B values of 0.69, 0.51, and 0.70, and higher M values of 0.15, 0.11, and 0.20.

It has been demonstrated that strain partitioning due to the presence of mica can affect CPO development in quartz-rich rocks (e.g., Starkey and Cutforth, 1978; Little et al., 2015), and can play a role in controlling the overall grain size of dynamically recrystallized quartz (i.e., Song and Ree, 2007; Herwegh et al., 2011). These effects are generally interpreted as the result of the predominant mechanism of quartz recrystallization in rocks with higher mica content (i.e., grain boundary sliding rather than grain boundary migration-induced dislocation creep; Starkey and Cutforth, 1978; Little et al., 2015). Additionally, Hunter et al. (2016b) demonstrated that a higher degree of interconnectivity between mica grains can decrease the overall strength of a quartz-bearing rock, even in areas of the sample where the mica grains are not in contact with quartz. Therefore, it is unsurprising that strain partitioning due to the presence of mica can also affect fabric intensity parameters (Larson et al., 2017;

Hunter et al., 2016b, 2019). To determine if mica content affected the cylindricity and M-indices of our samples, we calculated the area percentage of mica in thin sections of each EBSD sample (Figs. 3 and 5, Table 1, Supplementary Material Fig. S3). Mica area percentage ranged between 0 and 13.5% for the Puna Tsang Chu transect samples and 0.7–19.2% for the Sarpang transect samples. While the sample with the lowest fabric intensity (Sample 5A) did also have the highest measured mica percent area, comparison of the patterns of B and M values with mica area percentage from the rest of the samples does not demonstrate a correlation (i.e., low-mica samples yielded both high and low cylindricity, and vice versa; see Fig. S3).

6. Shear-sense and kinematic vorticity data

6.1. Shear-sense indicators

Multiple shear-sense indicators were observed in outcrops and in thin sections (Fig. 7) and were also defined by asymmetric quartz *c*-axis fabrics of several EBSD samples from the Puna Tsang Chu transect (Fig. 6). Shear-sense indicators were observed at all structural levels (Fig. 3) but are more abundant in proximity to the reference position of the MCT. Outcrop- and thin section-scale shear-sense indicators include quartz vein boudins sheared into sigma objects, delta and sigma clasts (typically plagioclase), SC fabrics, C′-type shear bands, mica fish, and asymmetric folds (Fig. 7). Overall, these features dominantly define top-to-the-south shear. Quartz *c*-axis pole plots of ten EBSD samples exhibit girdles that are inclined to the south, all defining a top-to-S shear sense. Only one sample (9B) exhibited a top-to-N single girdle. Samples from the Sarpang transect also exhibit a dominance of top-to-S shear-sense indicators (Fig. 5), as observed in outcrops, thin sections, and *c*-axis pole plots (Long et al., 2016).

6.2. Kinematic vorticity data

The mean kinematic vorticity number (W_m) is a dimensionless value between 0 and 1 which measures the ratio of pure to simple shear (e.g., Passchier, 1987; Tikoff and Fossen, 1993; Means, 1994). A W_m of 0 indicates entirely pure shear deformation, a W_m of 1 indicates entirely simple shear deformation, and values in between represent a combination of the two. Here, we used the quartz shape-preferred-orientation (SPO) method of Wallis (1992, 1995) to calculate W_m. This technique utilizes the angle between foliation and the center segment of the girdle on a quartz *c*-axis pole plot (β) combined with the angle between foliation and the dominant stretching direction of recrystallized quartz grains ($θ′_{ISA1}$) in a thin section of the same sample to calculate W_m (see SM for details on methods). W_m values were calculated from 11 of the 13 Puna Tsang Chu samples, which are spread between −525 m and +2000 m (Table 1, Fig. 6) (the structurally highest two samples, 24A and 31, did not yield girdle patterns necessary for calculating a β angle). W_m values are variable, and range between 0.07 and 0.78, which indicates a pure shear-dominant component that ranges between 45 and 100% (Law et al., 2004). W_m values do not exhibit any pattern with structural height (Fig. 3).

W_m values previously reported for the nine published Sarpang transect samples typically range between 0.00 and 0.40, indicating a higher component of pure shear deformation (70–100%; Table 1) (Long et al., 2016). The two new samples analyzed here (samples 7 and 8) did not yield pole plots suitable for calculation of β angles.

7. Peak and deformation temperature data

Temperature data on the Puna Tsang Chu transect were collected using Raman spectroscopy of carbonaceous material (RSCM) thermometry, opening angle thermometry of quartz *c*-axis plots, and semi-quantitative deformation temperature bracketing using quartz recrystallization microstructures.

Table 1
Summary of kinematic vorticity, cylindricity, and m-index from EBSD samples on the PTC and Sarpang transect.

Puna Tsang Chu Samples

Thin Section	Lithology	Unit	Structural Height Relative to the MCT (m)	P	G	R	Cylindricity	M-index	Mica %	β (deg)	θ′ ISA1 (±1 SE)	W_m	% Pure Shear
31A	quartzite	GHlmu	11722	0.27	0.10	0.63	0.37	0.02	0.0%	–	–	–	–
24A	quartzite	GHlmu	7622	0.30	0.22	0.48	0.52	0.12	5.5%	–	–	–	–
17C	quartzite	GHlml	2422	0.57	0.11	0.32	0.68	0.27	4.7%	20	−1 ± 3°	0.52–0.70	50–65%
10C	quartz vein	GHlml	4	0.60	0.33	0.07	0.93	0.34	0.0%	4	5 ± 1°	0.44–0.48	65–70%
9B	quartzite	Jaishidanda	−19	0.44	0.47	0.09	0.91	0.23	4.9%	13	−5 ± 1°	0.23–0.30	80–85%
10D	quartzite	Jaishidanda	−22	0.47	0.38	0.14	0.86	0.23	6.5%	16	7 ± 3°	0.63–0.78	40–55%
8A	quartzite	Jaishidanda	−40	0.51	0.39	0.10	0.90	0.29	4.8%	6	5 ± 2°	0.31–0.41	70–80%
7B	quartzite	Jaishidanda	−44	0.47	0.44	0.08	0.92	0.25	4.9%	14	9 ± 1°	0.69–0.75	45–50%
5A	quartzite	Jaishidanda	−157	0.21	0.38	0.41	0.59	0.08	13.5%	14	8 ± 2°	0.66–0.75	45–55%
4A	quartzite	Jaishidanda	−277	0.33	0.52	0.15	0.85	0.20	6.4%	6	5 ± 1°	0.33–0.40	70–80%
3A	quartzite	Jaishidanda	−307	0.15	0.46	0.39	0.61	0.08	9.1%	4	0 ± 2°	0.07–0.22	85–100%
2A	quartzite	Jaishidanda	−437	0.28	0.42	0.30	0.70	0.13	5.6%	6	4 ± 1°	0.28–0.37	70–80
1A	quartzite	Jaishidanda	−517	0.21	0.61	0.18	0.82	0.14	7.3%	14	8 ± 2°	0.62–0.74	45–55%

Sarpang Samples

Thin Section	Lithology	Unit	Structural Height Relative to the MCT (m)	P	G	R	Cylindricity	M-index	Mica %	β (deg)	θ′ ISA1 (±1 SE)	W_m	% Pure Shear
36	paragneiss	GHlml	200	0.48	0.23	0.30	0.70	0.20	18.5%	–	5 ± 3°	0.10–0.35	75–95%
31	quartzite	Jaishidanda	−25	0.36	0.16	0.48	0.52	0.11	0.9%	8°	9 ± 3°	0.30–0.50	65–80%
29A	quartzite	Jaishidanda	−75	0.37	0.31	0.31	0.69	0.15	10.3%	6°	−7 ± 4°	0.15–0.45	65–90%
23	quartzite	Jaishidanda	−550	0.16	0.23	0.61	0.39	0.04	19.2%	5°	2 ± 3	0.00–0.20	85–100%
21	quartzite	Jaishidanda	−675	0.33	0.22	0.45	0.55	0.11	4.9%	2°	5 ± 3°	0.10–0.35	75–95%
18	quartzite	Daling	−1300	0.12	0.26	0.62	0.38	0.03	4.3%	4°	6 ± 2°	0.20–0.35	75–85%
16	quartzite	Daling	−1700	0.18	0.29	0.53	0.47	0.05	8.2%	0°	−2 ± 2	0.00–0.20	85–100%
12	quartzite	Daling	−2175	0.08	0.23	0.68	0.32	0.02	0.7%	−5°	4 ± 3°	0.05–0.30	80–95%
10	quartzite	Daling	−2300	0.03	0.08	0.89	0.11	0.00	7.5%	0°	3 ± 3°	0.00–0.25	80–100%
8	quartzite	Manas	−2425	0.04	0.03	0.93	0.07	0.00	2.2%	–	–	–	–
7	quartzite	Manas	−2550	0.03	0.02	0.95	0.05	0.01	4.9%	–	–	–	–
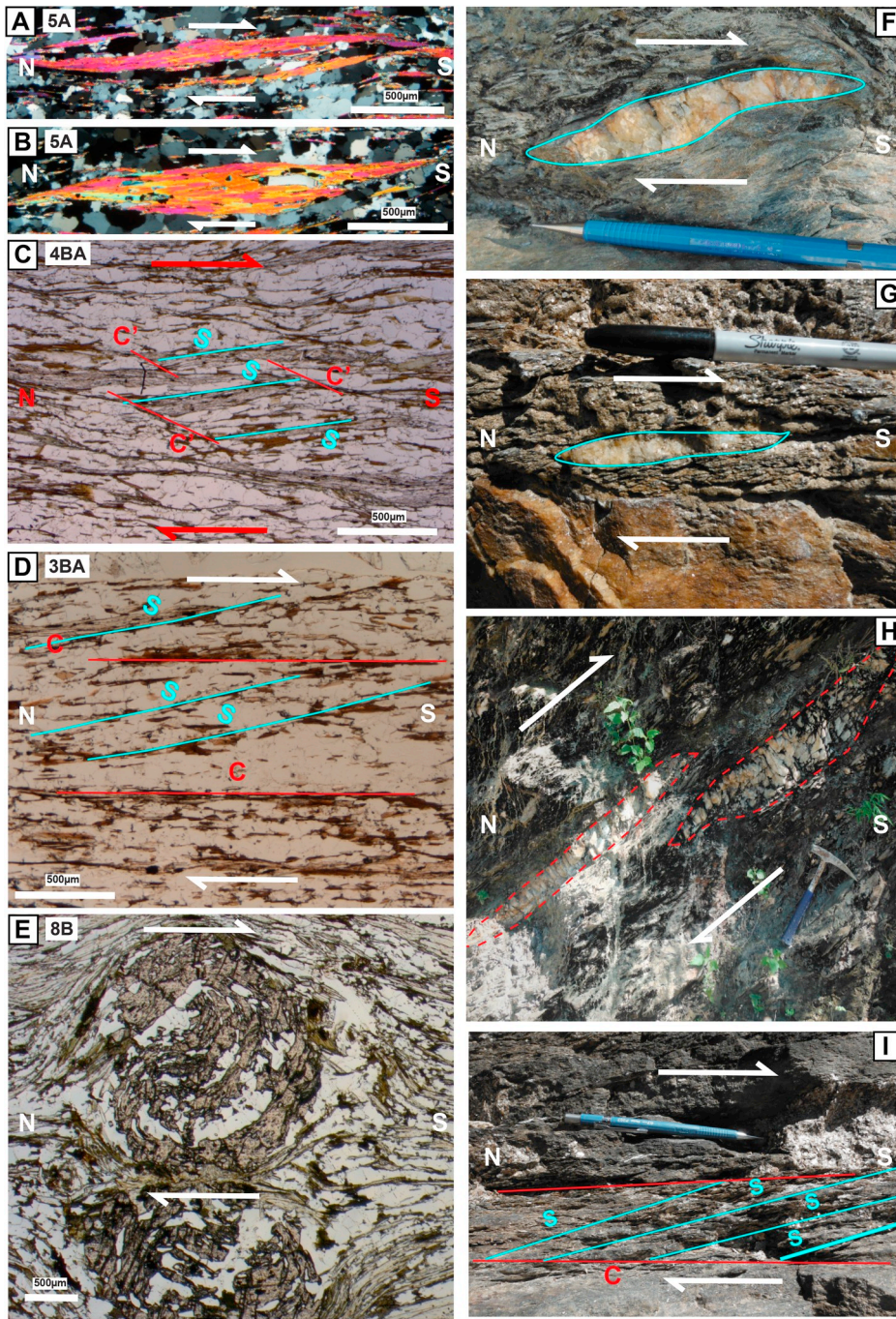
Fig. 7. Photographs and photomicrographs showing representative outcrop- and thin section-scale top-to-south shear-sense indicators observed on the Puna Tsang Chu transect. A-B) mica fish in sample 5A (XPL). C) C′-type shear band in sample 4BA (PPL). D) S–C fabric in sample 3BA (plane-polarized light; PPL). E) rotated garnet porphyroblast in sample 8B (PPL). F–H) Quartz vein boudins sheared into sigma objects; photo F taken near sample 2, photo G taken near sample 26, and photo H taken near sample 24. I) S–C fabric; photo taken near sample 24.

7.1. RSCM thermometry

The peak metamorphic temperature attained by a metasedimentary rock that contains organic matter can be measured using RSCM thermometry (e.g., Beyssac et al., 2002, 2003; Rahl et al., 2005). The relative heights and areas of four Raman peaks for carbonaceous material in the wavenumber offset range between 1200 and 1800 cm^{-1} have been calibrated to peak deformation temperatures between ~100 and ~740 °C (Rahl et al., 2005). RSCM temperatures from nine samples on the Puna Tsang Chu transect were measured using a spectrometer at the LeRoy Eyring Center for Solid State Science at Arizona State University (see SM for methodology and supporting data) (Fig. 3). Representative examples of analyzed carbonaceous material and Raman spectra are shown on Fig. 8, and mean RSCM temperatures (reported at the two standard error level) are summarized on Table 2. Four schist samples from the Jaishidanda Formation, collected at −520 m, −310 m, −285 m, and −160 m, yielded temperatures of 498 ± 31 °C, 519 ± 57 °C, 475 ± 37 °C, and 541 ± 36 °C, respectively (Fig. 3). Five GH samples, collected at +0.03, +3.3, +4.9, +9.0, and +10.6 km, yielded temperatures of 623 ± 83 °C, 646 ± 49 °C, 600 ± 47 °C, 615 ± 40 °C, and 689 ± 39 °C, respectively. Collectively, these data demonstrate a 125 ± 72 °C increase in peak temperature between 550 m below and 50 m above the reference position of the MCT, and approximately constant temperatures in GH rocks above.

Long et al. (2016) presented RSCM temperatures and garnet-biotite thermometry from the Sarpang transect, which demonstrated an upward increase from ~400 to 500 °C to ~700–750 °C between 675 m below and 200 m above the MCT (Fig. 5). Temperatures below and
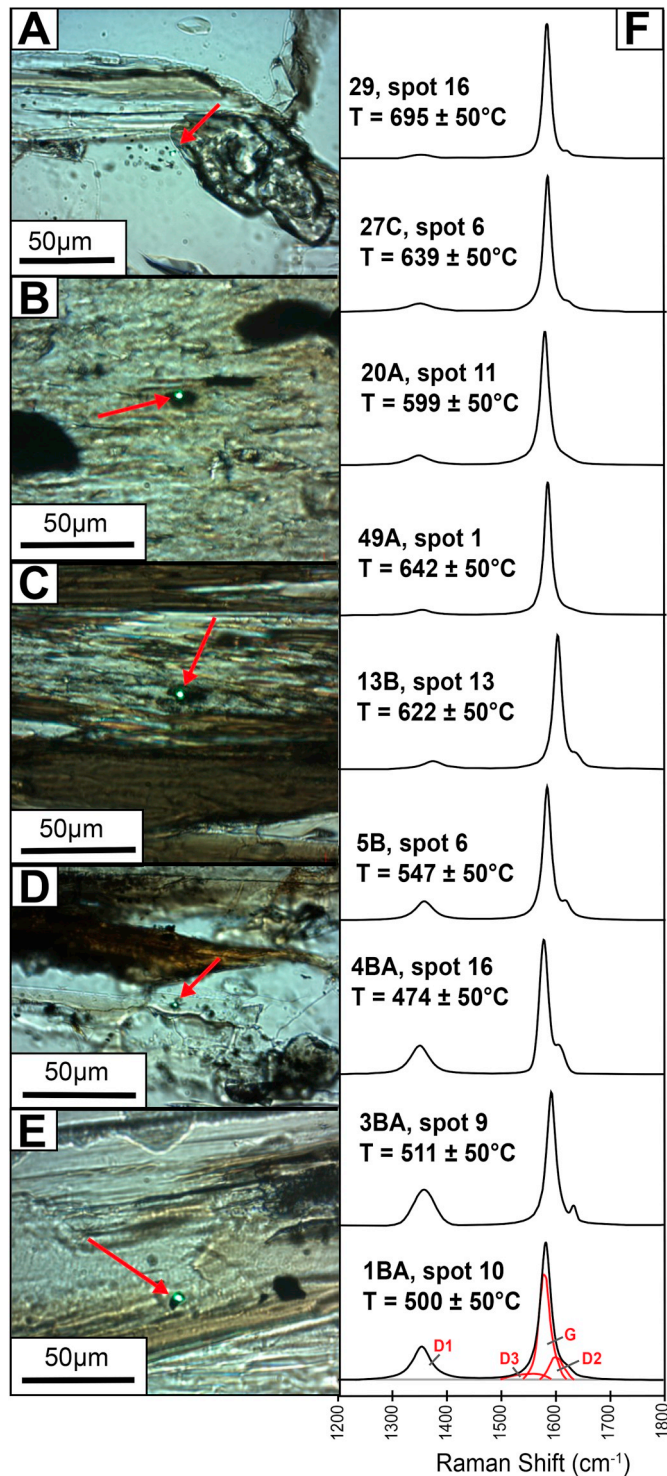
Fig. 8. A-E) Photomicrographs (PPL) of analyzed carbonaceous material (highlighted by red arrows). The green spot is the Raman laser beam. F) Representative examples of Raman spectra collected from Puna Tsang Chu transect samples, showing spot number and calculated temperature. Samples are arranged according to structural height, and positions of the graphite (G) and defect (D1, D2, D3) bands are shown on the lowest spectra. Single spot analyses are shown with ±50 °C uncertainty, which is the internal uncertainty from the Rahl et al. (2005) RSCM calibration.

above this interval were approximately constant at ~400–500 °C and ~650–700 °C, respectively (Long et al., 2016).

7.2. Quartz c-axis opening angle thermometry

The opening angle between the legs of a crossed-girdle pattern on a quartz *c*-axis pole plot has been demonstrated to increase proportional to the temperature at which the fabric was generated (e.g., Kruhl, 1998; Morgan and Law, 2004; Faleiros et al., 2016). Only one of the analyzed Puna Tsang Chu samples (3A; −310 m) yielded a crossed-girdle pattern (Fig. 3), which exhibits opening angles of 48°. Using the Faleiros et al. (2016) calibration, this corresponds to a deformation temperature of 380 ± 50 °C. On the Sarpang transect, Long et al. (2016) obtained opening angle temperatures from five quartzite samples distributed between −2.2 km and −0.7 km, which ranged from 54 to 64°, corresponding to deformation temperatures between ~400 and 500 °C (Fig. 5).

7.3. Deformation temperature ranges from quartz recrystallization microstructures

Approximate deformation temperature ranges can be estimated using optical analysis of dominant quartz recrystallization microstructures in thin sections (e.g., Stipp et al., 2002; Law, 2014), assuming the samples in question experienced a similar strain rate as those used to define the quartz recrystallization temperature thermometer calibrated for Himalayan rock samples by Law (2014). These mechanisms include: bulging (BLG), subgrain rotation (SGR), grain boundary migration (GBM), and chessboard extinction (CBE). BLG is characterized by small (≤10–20 μm) bulges or distinct subgrains localized at quartz boundaries. SGR recrystallization is characterized by equigranular, polygonal, ~20–50 μm subgrains. GBM recrystallization produces large (up to multiple mm size), cuspate, 'amoeboid' grains with characteristic interfingering boundaries, and CBE is indicated by multiple extinction domains intersecting at right angles within large, amoeboid quartz grains (e.g., Stipp et al., 2002). Temperature ranges calibrated for Himalayan rocks have been estimated as follows: BLG = ~350–450 °C, SGR = ~450–550 °C, GBM = ~550–650 °C (Law, 2014), and CBE = ~630–750 °C (not Himalayan specific) (Stipp et al., 2002).
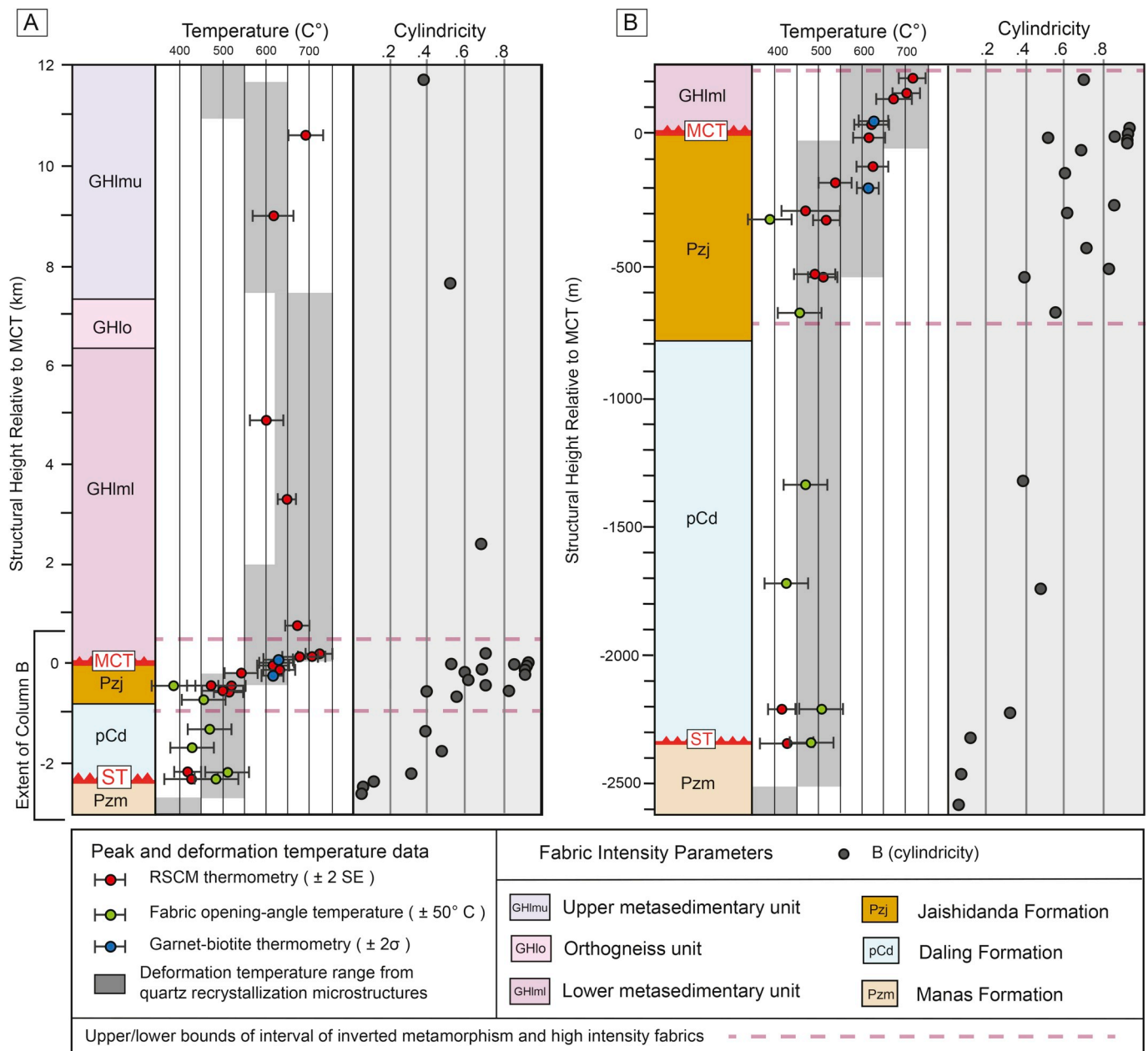
Quartz recrystallization observations provide the most comprehensive temperature data set for the Puna Tsang Chu transect. Jaishidanda Formation samples between −560 m and −460 m exhibit SGR microstructures, and between −460 m and −30 m exhibit either SGR microstructures, GBM microstructures, or an SGR-GBM transitional microstructure (Figs. 3 and 4). In the interval between −30 m and +4 m, samples primarily exhibit GBM microstructures, and between +4 m and +2000 m a combination of GBM and CBE microstructures were observed. Between +2.0 km and +8.0 km, GH rocks are dominated by CBE microstructures. Moving structurally higher, deformation temperatures then begin to decrease, with samples between +8.0 km and +11.0 km exhibiting GBM microstructures, and samples between +11.0 km and +12.0 km yielding SGR microstructures. Collectively, these observations define an upward increase in deformation temperature from ~450 to 550 °C to ~630–750 °C between −550 m and +4 m, approximately constant deformation temperatures of ~630–750 °C between +4 m and +8.0 km, and an upward decrease from ~630 to 750 °C to ~450–550 °C between +8.0 km and +12.0 km.

On the Sarpang transect (Fig. 5), Long et al. (2016) documented BLG-dominant recrystallization below the ST, SGR recrystallization between −2.2 and −0.6 km, GBM between −0.6 and −0.05 km, and CBE between −0.05 and + 0.7 km. This corresponds to an upward increase in deformation temperatures from ~450 to 550 °C to ~630–750 °C between −0.6 and −0.05 km, which closely parallels the inverted thermal field gradient exhibited by peak temperature data (Fig. 5).

Table 2
Summary of RSCM peak temperature determinations from Puna tsang Chu transect samples.

Thin Section	Lithology	Unit	Structural Height Relative to the MCT (m)	RI		R2		Peak Temperature (°C)			n
				Mean	1σ	Mean	1σ	Mean	1σ	2SE	
BU13-62	schisty quartzite	GHlmu	10,600	0.036	0.033	0.056	0.059	689	53	39	14
BU13–61C	qtzite	GHlmu	9000	0.049	0.030	0.128	0.063	615	60	40	15
BU13-56A	quartzite	GHlml	4900	0.073	0.029	0.150	0.070	600	67	47	13
BU13-75A	paragneiss	GHlml	3300	0.045	0.025	0.099	0.053	646	49	38	14
BU14-41B	schist	GHlml	28	0.078	0.075	0.129	0.098	623	83	41	22
BU14-45B	schist	Jaishidanda	−380	0.162	0.057	0.230	0.074	541	63	36	20
BU14-44BA	schist	Jaishidanda	−445	0.233	0.101	0.311	0.096	475	76	37	24
BU14-43BA	schist	Jaishidanda	−455	0.273	0.060	0.280	0.051	519	39	57	5
BU13–47B	schist	Jaishidanda	−560	0.195	0.047	0.280	0.041	498	33	31	15

Fig. 9. A) Simplified tectonostratigraphic column, which combines temperature and cylindricity data from the Puna Tsang Chu and Sarpang transects. MCT – Main Central thrust, ST, - Shumar thrust. B) Portion of the same tectonostratigraphic column as A, but zoomed in to the section between −2.6 km and +0.3 km.
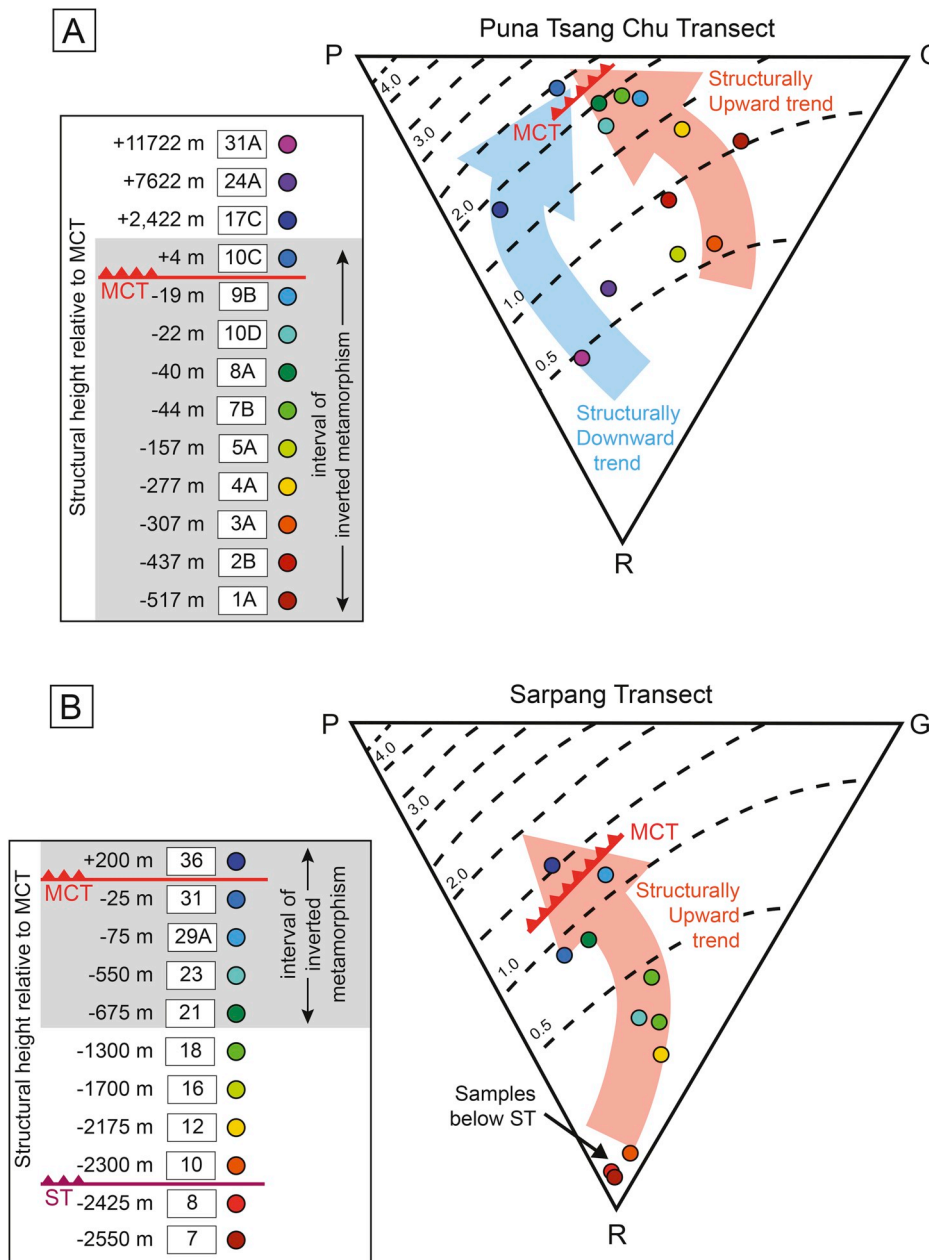
Fig. 10. Ternary plots showing point (P), girdle (G), and random (R) values for A) Puna Tsang Chu and B) Sarpang transect quartz fabric samples. Samples were plotted via the methods outlined by Vollmer (1990) and are shown with intensity contours as defined by Lisle (1985). Intensity contours increase toward the P fabric, and plotted samples demonstrate a transition to more ordered fabrics with proximity to the mapped position of the MCT. Key shows samples arranged via structural height, the mapped location of the MCT, and the interval of inverted metamorphism.

8. Discussion

Ongoing disagreements over how to best define shear zones within packages of rock that have been pervasively recrystallized impede our ability to accurately map and correlate shear zones in the Himalaya and elsewhere (e.g., Searle et al., 2008; Martin, 2016). Here, we integrate the fabric and temperature datasets discussed above to demonstrate that quartz fabric intensity parameters can help delineate spatial patterns of relative strain magnitude across the MCT in western Bhutan. We then explore implications for the application of this technique to other shear zones.

8.1. Integration of fabric, temperature, and structural datasets

The temperature and fabric intensity datasets for both the Puna Tsang Chu and Sarpang transects are graphed together on Fig. 9. In general, the deformation and peak temperature data at any given structural level overlap within error, which indicates that shearing and

associated recrystallization and fabric development took place while the rocks were at or near their peak temperature (e.g., Law, 2014; Long et al., 2016). Therefore, here we interpret the deformation and peak temperature datasets together, in order to define temperature patterns with structural level. The temperature data delineate a narrow (~900 m; between −700 m and +200 m) zone of inverted metamorphism that crosses the mapped reference location of the MCT. Temperatures increase upward from ~450 °C to ~725 °C in this interval. This zone of inverted metamorphism is corroborated by the structurally-upward appearance of garnet at −675 m (Fig. 5), and kyanite, gneissic banding, and leucosomes between −20 m and 0 m (Figs. 3 and 4). Above the MCT zone, between +0.2 and + 7.5 km, there is an interval of approximately constant (~600–750 °C) temperature and eventually a gradual upsection decrease to ~450–550 °C by +12 km. This correlates with the successive disappearance of kyanite, leucosomes, and garnet with increasing structural height between +8 km and +10 km (Fig. 3).

On both transects, a pattern of increasingly non-random fabrics with proximity to the mapped position of the MCT is also observed (Figs. 9

and 10). When fabric intensity data from both transects are plotted together, they define an interval of elevated intensity distributed through a structural thickness of ~900 m (Fig. 9). Cylindricity values above the ST increase upward from 0.11 to 0.47 between −2.3 km and −1.3 km. Between −0.7 km and +0.2 km, 15 samples exhibit cylindricity values that range between 0.55 and 0.93, with the highest values (0.86–0.93; n = 5) attained between −45 m and +5 m. The M-indices show similar trends as the B values. M-indices above the ST increase upward from 0.00 to 0.05 between −2.3 and −1.3 km. Between −0.7 km and +0.2 km, 15 samples exhibit M-indices that range between 0.11 and 0.20, with the highest values (0.23–0.34; n = 5) attained between −45 m and +5 m. The ~900 m-thick interval of elevated fabric intensity directly overlaps the interval of inverted metamorphism. Between +2.4 and + 11.7 km, three samples define an upward-decreasing trend in cylindricity and M-indices, with values decreasing from 0.68 to 0.37 and 0.27 to 0.02, respectively.

8.2. Interpretation of trends in fabric intensity, and some caveats

Many studies have established that finite strain magnitude is expected to increase with proximity to a shear zone, with the greatest strain predicted at the center of the zone (e.g., Ramsay, 1967; Ramsay, 1980; Simpson and De Paor, 1993; Evans and Dunne, 1991; Vitale and Mazzoli, 2009). Quantifiable measures of fabric strength can, in principle, be used as a proxy for relative strain magnitude because increased dynamic recrystallization and fabric development occurs with increased strain magnitude (e.g., Rahl and Skemer, 2016; Xia and Platt, 2018). Moreover, recent work has demonstrated that the non-randomness of quartz *c*-axis fabrics can be used to quantify the fabric strength of quartz-rich tectonites (e.g., Hunter et al., 2016b, 2018; Larson et al., 2017, 2018). The degree of non-randomness has been interpreted as a relative measure of finite strain magnitude and has been used to confirm qualitative field observations of strain adjacent to Himalayan shear zones (Larson et al., 2017, 2018; Hunter et al., 2018, 2019; Long et al., 2019). Our data demonstrate that fabric intensity increases with proximity to an uncontested location of the MCT, further demonstrating the viability of this approach.

Several additional caveats to this method merit further mention, namely that there should be negligible hydrolytic weakening (e.g., Blacic, 1975), no visible annealing of the quartz fabrics (e.g., Heilbronner and Tullis, 2002; Augenstein and Berg, 2011; Wilson et al., 2014), and an invariant strain rate (e.g., Kruhl, 1998; Morgan and Law, 2004; Faleiros et al., 2016). Furthermore, lithologically-controlled strain partitioning within shear zones can be a significant potential source for deviation from the predicted spatial patterns of finite strain (e.g., Sanderson, 1982; Ramsay and Huber, 1983; Evans and Dunne, 1991; Simpson and De Paor, 1993; Vitale and Mazzoli, 2009). In particular, strain partitioning within lithologies that contain a high-volume percentage of mica would be predicted to result in lower quartz fabric intensity when compared to proximal, low-mica, quartz-rich rocks (Hippertt, 1994; Tullis and Wenk, 1994; Larson and Cottle, 2014). Experiments have demonstrated that mica volume percentages of 25% or higher can greatly reduce the amount of dynamic recrystallization of quartz, mainly due to the overall decrease in contact area between quartz grains (Tullis and Wenk, 1994). For this reason, we selected samples that exhibited the lowest amount of mica for EBSD analysis. As discussed above, comparison of mica content from our EBSD samples with patterns of B and M values did not demonstrate a correlation (i.e., low-mica samples yielded both high and low cylindricity values and M-indices, and vice versa) (Figs. 3 and 5, Table 1, SM Fig. S3). This suggests that mica content in the analyzed samples did not significantly affect strain partitioning. Rather, we suggest that it is more likely that strain was partitioned into mica-rich lithologies that are interlayered on our studied transects, including schist and phyllite intervals within LH units, and schist and paragneiss intervals within GH units. As is it unknown how much of the overall strain was partitioned into the

micaceous intervals, the intensity parameters measured in our study should not be considered to represent absolute strain magnitude, but rather should be viewed as a means of determining spatial variation in relative finite strain magnitude. Overall, the trends defined by our fabric intensity parameters show a clearly defined interval of elevated intensity that we interpret as broadly representative of the spatial patterns of relative finite strain magnitude.

8.3. Implications for delineation of Himalayan shear zones

The importance of the MCT as a first-order structure in the Himalayan orogen is well established (e.g., Heim and Gansser, 1939; Gansser, 1964, 1983; LeFort, 1975; Searle et al., 2008; Martin, 2016). Decades of debate have centered on the ideal method for mapping the location of the MCT. As noted by Martin (2016) in his review of the various definitions of the MCT, consensus about how best to map this structure would greatly facilitate direct comparison of interpretations along the length of the orogen. Rather than provide a new, independent means of defining shear zone boundaries, we propose that the fabric intensity approach that we utilized is best implemented in conjunction with supporting datasets, including temperature measurements, shear-sense observations, and field observations of mineral assemblages and fabrics.

Our results for western Bhutan demonstrate that an interval of elevated quartz fabric intensity corresponds spatially with a ~900 m-thick zone of inverted metamorphism that surrounds the mapped reference location of the MCT. We argue that this zone of inverted metamorphism delineates the approximate upper and lower boundaries of the zone of high-magnitude shearing associated with MCT motion. Together, these datasets support the characterization of the MCT as a zone of higher strain and inverted metamorphism, rather than a discrete structure (e.g., Daniel et al., 2003; Long et al., 2016). This aligns with the widely accepted interpretation of the MCT as a shear zone (e.g., Martin, 2016), which inherently encompasses a thicker section of deformed rocks than a brittle thrust fault (e.g., Ramsay, 1980). Additionally, the fabric data presented here are consistent with the location of the MCT in Bhutan that has been mapped using differing criteria in multiple previous studies (e.g., Gansser, 1983; Bhargava, 1995; Grujic et al., 1996, 2002; Daniel et al., 2003; Long and McQuarrie, 2010; Long et al., 2011a, 2011c, 2016; Corrie et al., 2012).

Elsewhere in the orogen, the MCT has been mapped at the location of a metamorphic discontinuity (i.e., the contact between higher-grade rocks in the hanging wall and lower-grade rocks in the footwall; e.g., Gansser, 1964) or at the base of prominent recrystallization (e.g., Searle et al., 2008). Other studies have defined the MCT based on the age of shearing (e.g., Yin, 2006; Webb et al., 2013), the age of footwall metamorphism (e.g., Harrison et al., 1997), or on the isotopic compositions of sedimentary protoliths above and below (Ahmad et al., 2000; Martin et al., 2005). As demonstrated in Martin (2016), each of these definitions fails in some regions of the orogen, leaving no conclusive definition of the MCT that works everywhere. We suggest that by integrating quartz fabric intensity patterns with temperature and kinematic datasets, zones of high finite strain can be delineated in regions where the location of the MCT is debated. An ideal suite of datasets would include peak and deformation temperatures, shear-sense observations, field observations of metamorphic mineral assemblages and fabrics, and if possible, geochronology and pressure data as well.

This approach is suitable to application in other orogens where the locations of shear zones are difficult to constrain, provided the samples exhibit the ideal petrology (i.e., low mica content). Shear zones of potential interest for such a study would include the Monashee decollement (e.g., Brown et al., 1992; McNicoll and Brown, 1995) and Western Idaho Shear Zone (e.g., McClelland and Oldow, 2007; Tikoff et al., 2001) in the North American Cordillera, and the El Pichao shear zone in Argentina (Hunter et al., 2012; Hasalová et al., 2013), among others. In many cases, researchers have already conducted quantitative fabric analyses on quartz-rich tectonites in order to determine deformation

temperature and/or collect information about 3D strain (e.g., the data for the Sarpang transect from Long et al. (2016) that was utilized in this study, or, for example, data-rich studies such as Law et al., 2004, 2011; 2013). It is relatively simple to retroactively calculate quartz intensity parameters from existing fabric datasets, allowing this method to be implemented without additional sample collection.

9. Conclusions

1. Quartz fabric intensity values across the MCT define a ~900 m-thick interval of elevated intensity that corresponds spatially with an interval of inverted metamorphism. We suggest that the MCT is best described as a zone of higher strain and inverted metamorphism, and we interpret the upper and lower limits of intense fabrics to approximately delineate the boundaries of the high-strain MCT zone.

2. Patterns of fabric intensity with structural distance can be used as a proxy for relative finite strain magnitude; therefore, this approach has utility for delineating shear zones within thick packages of pervasively recrystallized rocks. Successful application of this method to a shear zone with an uncontested location, such as the MCT in western Bhutan, demonstrates its viability for constraining the spatial extents of contested shear zones in other orogens. We recommend applying this technique in conjunction with peak and deformation temperature data and kinematic observations.

CRediT authorship contribution statement

Jesslyn K. Starnes: Conceptualization, Software, Formal analysis, Investigation, Writing - original draft, Visualization. **Sean P. Long:** Conceptualization, Formal analysis, Investigation, Writing - original draft, Supervision, Funding acquisition. **Stacia M. Gordon:** Resources, Writing - review & editing, Funding acquisition. **Jingyi Zhang:** Methodology, Resources, Formal analysis, Investigation, Writing - original draft. **Emmanuel Soignard:** Methodology, Resources, Formal analysis.

Acknowledgements

Appendix A. Supplementary data

Supplementary data related to this article can be found at https://doi.org/10.1016/j.jsg.2019.103941.

References

Ahmad, T., Harris, N., Bickle, M., Chapman, H., Bunbury, J., Prince, S., 2000. Isotopic constraints on the structural relationships between the lesser Himalayan series and the high Himalayan crystalline series, Garhwal Himalaya. Geol. Soc. Am. Bull. 112 (3), 467–477.

Allmendinger, R.W., Cardozo, N., Fisher, D., 2011. Structural geology algorithms: Vectors and tensors in structural geology. Cambridge University Press, New York.

Augenstein, C., Berg, J., 2011. Natural annealing of dynamically recrystallized quartzite fabrics: examples from the Cévennes, SE French Massif Central. J. Struct. Geol. 33 (3), 244–254.

Bachmann, F., Hielscher, R., Schaeben, H., 2010. Texture analysis with MTEX – Free and open source software toolbox. Solid State Phenom. 160, 63–68.

Barnhoorn, A., Bystricky, M., Burlini, L., Kunze, K., 2004. The role of recrystallisation on the deformation behaviour of calcite rocks: large strain torsion experiments on Carrara marble. J. Struct. Geol. 26 (5), 885–903.

Barth, N., Hacker, B., Seward, G., Walsh, E., Young, D., Johnston, S., 2010. Strain within the Ultrahigh Pressure Western Gneiss Region of Norway Recorded by Quartz CPOs: Geological Society Special Publications, vol. 335, pp. 663–685.

Bhargava, O.N., 1995. The Bhutan Himalaya: A Geological Account, vol. 39. Special Publication of the Geological Survey of India, pp. 1–245.

Beyssac, O., Goffe, B., Chopin, C., Rouzaud, J., 2002. Raman spectra of carbonaceous material in metasediments: a new geothermometer. J. Metamorph. Geol. 20, 859–871.

Beyssac, O., Goffe, B., Petitet, J.P., Froigneux, E., Moreau, M., Rouzaud, J.N., 2003. On the characterization of disordered and heterogeneous carbonaceous materials by Raman spectroscopy. Acta A Mol. Biomol. Spectrosc. 59, 2267–2276.

Bhattacharya, A.R., Weber, K., 2004. Fabric development during shear deformation in the Main central thrust zone, NW-Himalaya, India. Tectonophysics 387, 23–46.

Blacic, J.D., 1975. Plastic deformation mechanisms in quartz: the effect of water. Tectonophysics 27, 271–294.

Bouchez, J.L., 1978. Preferred orientations of quartz <a> axes in some tectonites: kinematic inferences. Tectonophysics 49 (1–2), T25–T30.

Bouchez, J.L., Pecher, A., 1981. The Himalayan Main central thrust pile and its quartz-rich tectonites in central Nepal. Tectonophysics 78 (1–4), 23–50.

Bouchez, J.L., Lister, G.S., Nicolas, A., 1983. Fabric asymmetry and shear sense in movement zones. Geol. Rundsch. 72 (2), 401–419.

Brown, R.L., Carr, S.D., Johnson, B.J., Coleman, V.J., Cook, F.A., Varsek, J.L., 1992. The Monashee decollement of the southern Canadian Cordillera: a crustal-scale shear zone linking the Rocky Mountain Foreland belt to lower crust beneath accreted terranes. Thrust Tectonics. Springer, Dordrecht.

Bunge, H.J., 1982. Texture Analysis in Materials Science: Mathematical Models. Butterworths, London.

Carreras, J., Garcia Celma, A., 1982. Quartz of c-axis fabric variation at the margins of a shear zone developed in schists from Cap de Creus (Spain). Acta Geol. Hisp. 17 (3), 137–149.

Dasgupta, S., 1995. Shumar formation. In: Bhargava, O.N. (Ed.), The Bhutan Himalaya: A Geological Account, vol. 39. Geological Society of India Special Publication, Calcutta, India, pp. 64–78.

Catlos, E.J., Harrison, T.M., Kohn, M.J., Grove, M., Ryerson, F.J., Manning, C.E., Upreti, B.N., 2001. Geochronologic and thermobarometric constraints on the evolution of the Main Central Thrust, central Nepal Himalaya. J. Geophys. Res. 106, 16177–16204.

Corrie, S.L., Kohn, M.J., McQuarrie, N., Long, S.P., 2012. Flattening the Bhutan Himalaya. Earth Planet. Sci. Lett. 349–350, 67–74.

Daniel, C.G., Hollister, L.S., Parrish, R.R., Grujic, D., 2003. Exhumation of the Main central thrust from lower crustal depths, eastern Bhutan Himalaya. J. Metamorph. Geol. 21, 317–334.

Evans, M.A., Dunne, W.M., 1991. Strain factorization and partitioning in the North Mountain thrust sheet, central Appalachians, U.S.A. J. Struct. Geol. 13, 21–35.

Faleiros, F.M., Moraes, R., Pavan, M., Campanha, G.A.C., 2016. A new empirical calibration of the quartz c-axis fabric opening-angle deformation thermometer. Tectonophysics 671, 173–182.

Gansser, A., 1964. Geology of the Himalayas. Wiley-Interscience, New York.

Gansser, A., 1983. Geology of the Bhutan Himalaya. Birkauser, Basel, Switzerland.

Grujic, D., Casey, M., Davidson, C., Hollister, L., Kundig, R., Pavlis, T.L., Schmid, S., 1996. Ductile extrusion of the Higher Himalayan Crystalline in Bhutan: Evidence from quartz microfabrics. Tectonophysics 260, 21–43.

Grujic, D., Hollister, L.S., Parrish, R.R., 2002. Himalayan metamorphic sequence as an orogenic channel: insight from Bhutan. Earth Planet. Sci. Lett. 198, 177–191.

Harrison, T.M., Ryerson, F.J., LeFort, P., Yin, A., Lovera, O., Catlos, E.J., 1997. A late Miocene–Pliocene origin for the central Himalayan inverted metamorphism. Earth Planet. Sci. Lett. 146, E1–E7.

Hasalová, Pavlína, Hunter, Nicholas, Weinberg, Roberto, Finch, Melanie, 2013. Clast Rotation and Nature of Strain Localization in Thick Ultramylonites: the El Pichao Shear Zone (Sierra de Quilmes), NW Argentina. Abstract presented at the European Geological Union Annual Assembly, Vienna, Austria.

Heilbronner, R., Tullis, J., 2002. The effect of static annealing on microstructure and crystallographic preferred orientations of quartzites experimentally deformed in axial compression and shear. In: de Meer, S., et al. (Eds.), Deformation Mechanisms, Rheology and Tectonics: Current Status and Future Perspectives, vol. 200. Geological Society of American Special Publication, pp. 191–218.

Heilbronner, R., Tullis, J., 2006. Evolution of c-axis pole figures and grain size during dynamic recrystallization: Results from experimentally sheared quartzite. J. Geophys. Res.: Solid Earth 111 (B10), B10202.

Heim, A., Gansser, A., 1939. Central Himalayan Geology. Geologic Observations of Swiss Expedition, 1936.

Herwegh, M., Linckens, J., Ebert, A., Berger, A., Brodhag, S.H., 2011. The role of second phases for controlling microstructural evolution in polymineralic rocks: a review. J. Struct. Geol. 33 (12), 1728–1750.

Hippertt, J.F., 1994. Microstructures and c-axis fabrics indicative of quartz dissolution in sheared quartzites and phyllonites. Tectonophysics 229, 141–163.

Hunter, Nicholas, Hasalová, Pavlína, Weinberg, Roberto, Finch, Melanie, 2012. Clast Rotation and the Origin of Thick Ultramylonites: the El Pichao Shear Zone (Sierra de Quilmes), NW Argentina. Abstract presented at the American Geophysical Union Annual Meeting, San Francisco.

Hunter, N.J.R., Hasalova, P., Weinberg, R., Wilson, C.J.L., Luzin, V., 2016a. Using the 'crystal Signature' of Mylonites to Demarcate the Main Central Thrust (Alaknanda Region, Garhwal Himalaya). Abstract for Himalayan-Karakorum-Tibet Workshop, Dehradun, India.

Hunter, N.J.R., Hasalova, P., Weinberg, R., Wilson, C.J.L., 2016b. Fabric controls on strain accommodation in naturally deformed mylonites: the influence of interconnected micaceous layers. J. Struct. Geol. 83, 180–193.

Hunter, N.J.R., Weinberg, R.F., Wilson, C.J.L., Luzin, V., Misra, S., 2018. Microscopic anatomy of a 'hot-on-cold' shear zone: insights from quartzites of the Main Central Thrust in the Alaknanda region (Garhwal Himalaya). Geol. Soc. Am. Bull. 130, 1519–1539.

Hunter, N.J.R., Weinberg, R.F., Wilson, C.J.L., Luzin, V., Misra, S., 2019. Quartz deformation across interlayered monomineralic and polymineralic rocks: A comparative analysis. J. Struct. Geol. 119, 118–134.

Knipe, R.J., Law, R.D., 1987. The influence of crystallographic orientation and grain boundary migration on microstructural and textural evolution in an S-C mylonite. Tectonophysics 135 (1), 155–169.

Kruhl, J.H., 1998. Reply: prism- and basal-plane parallel subgrain boundaries in quartz: a microstructural geothermobarometer. J. Metamorph. Geol. 16, 142–146.

Larson, K.P., Cottle, J.M., 2014. Midcrustal discontinuities and the assembly of the Himalayan midcrust. Tectonics 33, 718–740.

Larson, K.P., Cottle, J., Lederer, G., Rai, S.M., 2017. Defining shear zone boundaries using fabric intensity gradients: An example from the east-central Nepal Himalaya. Geosphere 13, 771–781.

Larson, K., Ambrose, T.K., Webb, A.A.G., Cottle, J., Shrestha, S., 2018. Reconciling Himalayan midcrustal discontinuities: The Main Central thrust system. Earth Planet. Sci. Lett. 429, 139–146.

Law, R.D., Schmid, S.M., Wheeler, J., 1990. Simple shear deformation and quartz recrystallization fabrics: a possible natural example from the Torridon area of NW Scotland. J. Struct. Geol. 12, 29–45.

Law, R.D., Searle, M.P., Simpson, R.L., 2004. Strain, deformation temperatures and vorticity of flow at the top of the Greater Himalayan Slab, Everest Massif, Tibet. J. Geol. Soc. Lond. 161, 305–320.

Law, R.D., Jessup, M.J., Searle, M.P., Francsis, M.K., Waters, D.J., Cottle, J.M., 2011. Telescoping of isotherms beneath the South Tibetan Detachment System, Mount Everest Massif. J. Struct. Geol. 33, 1569–1594.

Law, R.D., Stahr, D.W., Francsis, M.K., Ashley, K.T., Grasemann, B., Ahmad, T., 2013. Deformation temperatures and flow vorticities near the base of the Greater Himalayan Series, Sutlej Valley and Shimla Klippe, NW India. J. Struct. Geol. 54, 21–53.

Law, R.D., 2014. Deformation thermometry based on quartz c-axis fabrics and recrystallization microstructures: A review. J. Struct. Geol. 66, 129–161.

Leech, M.L., Singh, S., Jain, A.K., Klemperer, S.L., Manichavasgam, R.M., 2005. The onset of India-Asia continental collision: Early, steep subduction required by the timing of UHP metamorphism in the western Himalaya. Earth Planet. Sci. Lett. 234, 83–97.

LeFort, P., 1975. Himalayas: The collided range. Present knowledge of the continental arc. Am. J. Sci. 275-A, 1–44.

Lisle, R.J., 1985. Geological Strain Analysis: A Manual for the Rf/φ Technique. Pergamon Press, New York.

Lister, G.S., 1977. Crossed-girdle c-axis fabrics in quartzite plastically deformed by plane strain and progressive simple shear. Tectonophysics 39, 51–54.

Lister, G.S., Hobbs, B.E., 1980. The simulation of fabric development during plastic deformation and its application to quartzite: The influence of deformation history. J. Struct. Geol. 2, 355–370.

Little, T.A., Prior, D.J., Toy, V.G., Lindroos, Z.R., 2015. The link between strength of lattice preferred orientation, second phase content and grain boundary migration: A case study from the Alpine Fault zone, New Zealand. J. Struct. Geol. 81, 59–77.

Long, S., McQuarrie, N., Tobgay, T., Rose, C., Gehrels, G., Grujic, D., 2011a. Tectonostratigraphy of the Lesser Himalaya of Bhutan: Implications for the along-strike stratigraphic continuity of the northern Indian margin. Geol. Soc. Am. Bull. 123, 1406–1426.

Long, S., McQuarrie, N., Tobgay, T., Grujic, D., Hollister, L., 2011b. Geologic map of Bhutan. J. Maps 7, 184–192.

Long, S., McQuarrie, N., Tobgay, T., Grujic, D., 2011c. Geometry and crustal shortening of the Himalayan fold-thrust belt, eastern and central Bhutan. Geol. Soc. Am. Bull. 123, 1427–1447.

Long, S.P., McQuarrie, N., 2010. Placing limits on channel flow: Insights from the Bhutan Himalaya. Earth Planet. Sci. Lett. 290, 375–390.

Long, S.P., McQuarrie, N., Tobgay, T., Coutand, I., Cooper, F.J., Reiners, P.W., Wartho, J., Hodges, K.V., 2012. Variable shortening rates in the eastern Himalayan thrust belt, Bhutan: insights from multiple thermochronologic and geochronologic datasets tied to kinematic reconstructions. Tectonics 31 (TC5004), 1–23.

Long, S.P., Gordon, S.M., Young, J.P., Soignard, E., 2016. Temperature and strain gradients through Lesser Himalayan rocks and across the Main Central thrust, south-central Bhutan: Implications for transport-parallel stretching and inverted metamorphism. Tectonics 35, 1863–1891.

Long, S.P., Mullady, C.L., Starnes, J.K., Gordon, S.M., Larson, K.P., Pianowski, L.S., Miller, R.B., Soignard, Emmanuel, 2019. A structural model for the South Tibetan detachment system in northwestern Bhutan from integration of temperature, fabric, strain, and kinematic data. Lithosphere 11 (4), 465–487.

Mainprice, D., Bachmann, F., Hielscher, R., Schaeben, H., 2015. Descriptive Tools for the Analysis of Texture Projects with Large Datasets Using MTEXC: Strength, Symmetry and Components, 409. Geological Society of London, Special Publications, pp. 251–271.

Martin, A.J., DeCelles, P.G., Gehrels, G.E., Patchett, P.J., Isachsen, C., 2005. Isotopic and structural constraints on the location of the Main Central thrust in the Annapurna Range, central Nepal Himalaya. Geol. Soc. Am. Bull. 117 (7–8), 926–944.

Martin, A.J., 2016. A review of definitions of the Himalayan Main Central Thrust. Int. J. Earth Sci. 106, 2131–2145.

Mattauer, M., 1986. Intracontinental subduction, crust-mantle décollement and crustal-stacking wedge in the Himalayas and other collision belts. In: Coward, M.P., Ries, A. C. (Eds.), Collision Tectonics, vol. 19. Geological Society of London Special Publication, pp. 37–50.

McClelland, W.C., Oldow, J.S., 2007. Late Cretaceous truncation of the western Idaho shear zone in the central North American Cordillera. Geology 35, 723–726.

McQuarrie, N., Robinson, D., Long, S., Tobgay, T., Grujic, D., Gehrels, G., Ducea, M., 2008. Preliminary stratigraphic and structural architecture of Bhutan: Implications for the along-strike architecture of the Himalayan system. Earth Planet. Sci. Lett. 272, 105–117.

McNicoll, V., Brown, R.L., 1995. The Monashee décollement at Cariboo Alp, southern flank of the Monashee complex, southern British Columbia, Canada. J. Struct. Geol. 17 (1), 17–30.

McQuarrie, N., Long, S.P., Tobgay, T., Nesbit, J.N., Gehrels, G., Ducea, M., 2013. Documenting basin scale, geometry and provenance through detrital geochemical data: Lessons from the Neoproterozoic to Ordovician Lesser, Greater, and Tethyan Himalayan strata of Bhutan. Gondwana Res. 23, 1491–1510.

McQuarrie, N., Tobgay, T., Long, S.P., Reiners, P.W., Cosca, M.A., 2014. Variable exhumation rates and variable displacement rates: Documenting recent slowing of Himalayan shortening in western Bhutan. Earth Planet. Sci. Lett. 386, 161–174.

Means, W.D., 1994. Rotational quantities in homogeneous flow and the development of small-scale structures. J. Struct. Geol. 17, 893–896.

Morgan, S., Law, R.D., 2004. Unusual transition in quartzite dislocation creep regimes and crystal slip systems in the aureole of the Eureka Valley-Joshua Flat-Beer Creek pluton, California: A case for anhydrous conditions created by decarbonation reactions. Tectonophysics 384, 209–231.

Muto, J., Hirth, G., Heilbronner, R., Tullis, J., 2011. Plastic anisotropy and fabric evolution in sheared and recrystallized quartz single crystals. J. Geophys. Res.: Solid Earth 116 (B2), B02206.

Najman, Y., 2006. The detrital record of orogenesis: A review of approaches and techniques used in the Himalayan sedimentary basins. Earth Sci. Rev. 74, 1–72.

Najman, Y., Allen, R., Willett, E.A.F., Carter, A., Barfod, D., Garzanti, E., Wijbrans, J., Bickle, M.J., Vezzoli, G., Ando, S., Oliver, G., Uddin, M.J., 2012. The record of Himalayan erosion preserved in the sedimentary rocks of the Hatia Trough of the Bengal Basin and the Chittagong Hill Tracts, Bangladesh. Basin Res. 24, 499–519.

Passchier, C.W., 1987. Stable positions of rigid objects in non-coaxial flow – a study in vorticity analysis. J. Struct. Geol. 124, 211–222.

Passchier, C.W., Trouw, R.A.J., 2005. Micro-tectonics, second ed. Springer, New York.

Pennacchioni, G., Menegon, L., Leiss, B., Bromiley, G., 2010. Development of crystallographic preferred orientation and microstructure during plastic deformation of natural coarse-grained quartz veins. J. Geophys. Res. 115 (12), 1–23.

Rahl, J.M., Anderson, K.M., Brandon, M.T., Fassoulas, C., 2005. Raman spectroscopic carbonaceous material thermometry of low-grade metamorphic rocks: Calibration and application to tectonic exhumation in Crete, Greece. Earth Planet. Sci. Lett. 240, 339–354.

Rahl, J.M., Skemer, P., 2016. Microstructural evolution and rheology of quartz in a mid-crustal shear zone. Tectonophysics 680, 129–139.

Ramsay, J.G., 1967. Folding and Fracturing of Rocks. McGraw Hill, New York.

Ramsay, J.G., 1980. Shear zone geometry: a review. J. Struct. Geol. 2, 83–99.

Ramsay, J.G., Graham, R.H., 1970. Strain variation in shear belts. Can. J. Earth Sci. 7 (3), 786–813.

Ramsay, J.G., Huber, M.I., 1983. The Techniques of Modern Structural Geology. Academic Press, New York.

Richards, A., Parrish, R., Harris, N., Argles, T., Zhang, L., 2006. Correlation of lithotectonic units across the eastern Himalaya, Bhutan. Geology 34, 341–344.

Robinson, D.M., DeCelles, P.G., Garzione, C.N., Pearson, O.N., Harrison, T.M., Catlos, E. J., 2001. The kinematic evolution of the Nepalese Himalaya interpreted from Nd isotopes. Earth Planet. Sci. Lett. 192, 507–521.

Robinson, D.M., DeCelles, P.G., Copeland, P., 2006. Tectonic evolution of the Himalayan thrust belt in western Nepal: implications for channel flow models. Geol. Soc. Am. Bull. 118, 865–885.

Rowley, D.B., 1996. Age of initiation of collision between India and Asia: A review of stratigraphic data. Earth Planet. Sci. Lett. 145, 1–13.

Sanderson, D.J., 1982. Models of strain variation in nappes and thrust sheets: a review. Tectonophysics 88, 201–233.

Searle, M.P., Law, R.D., Godin, L., Larson, K.P., Streule, M.J., Cottle, J.M., Jessup, M.J., 2008. Defining the Himalayan Main Central Thrust in Nepal. J. Geol. Soc. Lond. 165, 523–534.

Simpson, C., De Paor, D., 1993. Strain and kinematic analysis in general shear zones. J. Struct. Geol. 15, 1–20.

Skemer, P., Katayama, I., Jiang, Z., Karato, S.-I., 2005. The misorientation index: development of a new method for calculating the strength of lattice-preferred orientation. Tectonophysics 411, 157–167.

Song, W.J., Ree, J.H., 2007. Effect of mica on the grain size of dynamically recrystallized quartz in a quartz-muscovite mylonite. J. Struct. Geol. 29 (12), 1872–1881.

Starkey, J., Cutforth, C., 1978. A demonstration of the interdependence of the degree of quartz preferred orientation and the quartz content of deformed rocks. Can. J. Earth Sci. 15 (5), 841–847.

Stipp, M., Stunitz, H., Heilbronner, R., Schmid, S., 2002. The eastern Tonale fault zone: a natural laboratory for crystal plastic deformation of quartz over a temperature range from 250 to 700 °C. J. Struct. Geol. 24, 1861–1884.

Tangri, S.K., 1995. Baxa Group. In: Bhargava, O.N. (Ed.), The Bhutan Himalaya: A Geological Account, vol. 39. Geological Society of India Special Publication, pp. 38–58.

Tikoff, B., Fossen, H., 1993. Simultaneous pure and simple shear: the unifying deformation matrix. Tectonophysics 217, 267–283.

Tikoff, B., Kelso, P., Manduca, C.A., Markley, M.J., Gillaspy, J., 2001. Lithospheric and Crustal Reactivation of an Ancient Plate Boundary: the Assembly and Disassembly of the Salmon River Suture Zone, Idaho, USA, vol. 186. Geological Society, London, pp. 213–231. Special Publications.

Tobgay, T., McQuarrie, N., Long, S.P., Kohn, M.J., Corrie, S., 2012. The age and rate of displacement along the Main Central Thrust in the western Bhutan Himalaya. Earth Planet. Sci. Lett. 319, 146–158.

Tullis, J., Wenk, H.R., 1994. Effect of muscovite on the strength and lattice preferred orientations of experimentally deformed quartz aggregates. Mater. Sci. Eng. A 174, 209–220.

Vitale, S., Mazzoli, S., 2009. Finite strain analysis of a natural ductile shear zone in limestones: Insights into 3-D coaxial vs. non-coaxial deformation partitioning. J. Struct. Geol. 31, 104–113.

Vollmer, F.W., 1990. An application of eigenvalue methods to structural domain analysis. Geol. Soc. Am. Bull. 102, 786–791.

Wallis, S.R., 1992. Vorticity analysis in a metachert from the Sanbagawa Belt, SW Japan. J. Struct. Geol. 14, 271–280.

Wallis, S.R., 1995. Vorticity analysis and recognition of ductile extension in the Sanbagawa belt, SW Japan. J. Struct. Geol. 17, 1077–1093.

Webb, A.A.G., Yin, A., Dubey, C.S., 2013. U-pb Zircon Geochronology of Major Lithologic Units in the Eastern Himalaya: Implications for the Origin and Assembly of Himalayan Rocks, vol. 125. Geological Society of America Bulletin, pp. 499–522.

Wilson, C.J.L., Peternell, M., Piazolo, S., Luzin, V., 2014. Microstructure and fabric development in ice: lessons learned from in situ experiments and implications for understanding rock evolution. J. Struct. Geol. 61, 50–77.

Whitney, D.L., Evans, B.W., 2010. Structural geology algorithms: 723 Vectors and tensors in structural geology. Am. Mineral. 95, 185–187.

Wilson, C.J.L., Hunter, N.J.R., Luzin, V., Peternell, M., Piazolo, S., 2019. The influence of strain rate and presence of dispersed second phases on the deformation behaviour of polycrystalline D2O ice. J. Glaciol. 101–122.

Xia, H., Platt, J.P., 2018. Quartz grainsize evolution during dynamic recrystallization across a natural shear zone boundary. J. Struct. Geol. 109, 120–126.

Yin, A., Harrison, T.M., 2000. Geologic evolution of the Himalayan-Tibetan orogen. Annu. Rev. Earth Planet Sci. 28, 211–280.

Yin, A., 2006. Cenozoic tectonic evolution of the Himalayan orogen as constrained by along-strike variation of structural geometry, exhumation history, and foreland sedimentation. Earth Sci. Rev. 76, 1–131.